© 2011 by David C. Mertens

POPULATION-SPECIFIC PREDICTIONS FOR THE FINITE KURAMOTO MODEL AND COLLECTIVE SYNCHRONIZATION IN A SYSTEM WITH RESONANT COUPLING

BY

DAVID C. MERTENS

DISSERTATION

Submitted in partial fulfillment of the requirements
for the degree of Doctor of Philosophy in Physics
in the Graduate College of the
University of Illinois at Urbana-Champaign, 2011

Urbana, Illinois

Doctoral Committee:

Associate Professor Karin Dahmen, Chair
Professor Richard Weaver, Director of Research
Associate Professor Matthias Grosse Perdekamp
Assistant Professor Raffi Budakian

Abstract

Synchronization of coupled simple harmonic oscillators is a well-studied problem in advanced undergraduate mechanics courses and the solution amounts to solving an eigenvalue problem. Synchronization of populations of auto-oscillators is a comparatively new field of study. The first scientists to consider such problems were mathematical biologists, but applied mathematicians and physicists have made significant contributions as well. The chief model of synchronization of distinct auto-oscillators is due to Kuramoto. The most striking feature of the model is the presence of a phase transition from an unsynchronized to a partially synchronized state at a critical value of the inter-oscillator coupling. Also, in spite of being a microscopic model that describes the interactions between individual oscillators, Kuramoto's model can be recast exactly as a mean field model. A great deal of work has focused on predicting the behavior of the mean field.

The first part of this dissertation describes my work exploring the Kuramoto model. Most physicists have approached the problem by analyzing the behavior of infinitely sized systems. I focus instead on making precise predictions for specific, finitely sized populations of oscillators. In particular, I demonstrate that the assumption of a constant mean field leads to surprisingly good self-consistent predictions for the mean field, particularly if the frequency of synchronization is made a tunable parameter. However, I find that the discontinuities in the self-consistent predictions do not exhibit critical scaling, in contradiction with the known critical behavior exhibited by the Kuramoto model.

The second part of this dissertation describes laboratory work and modeling of a mechanical system that exhibits synchronization. I examine the synchronization of 16 cell-phone

vibrators coupled through a resonant plate. In light of the Kuramoto model, the interactions between the motors and the plate give somewhat unexpected results including bistability as well as ranges of frequencies in which the system never synchronize. I show, by starting with a first-principles model of the motors interacting with the plate, that the motors' interaction is similar to Kuramoto's model with two key differences: frequency-dependent coupling and a frequency-dependent phase delay.

To my parents

Acknowledgments

I would not be in the position of writing this dissertation were it not for my adviser, Richard Weaver. His wellspring of ideas coupled with an unending patience and a perpetually open door gave me the support and freedom to transition from being a student to being a scientist.

I owe a great deal to Karin Dahmen and her group members Braden Brinkman, Georgios Tsekenis, and Nir Friedman for teaching me how to prepare and study a scaling collapse. Their guidance made an otherwise confusing concept straightforward. Tyler Earnest, also in Professor Dahmen's group, helped me overcome a hurdle in automating my experimental system, and is a good friend.

The first paper is the hardest to write, and I wish to thank Nick Wolff for making a careful reading of my paper and giving helpful feedback. His feedback and encouragement helped me finish and submit a paper which took longer than I would have liked.

I have reached the upper echelons of academia because my parents and my grandparents have always impressed upon me the importance of a good education. My family has always encouraged the pursuit of excellence and knowledge and this dissertation is the culmination of that pursuit.

Finally, I appreciate the love, support, and patience, of my fiancée Katherine, especially as I prepared this dissertation. It took longer than we had hoped, but it is finally done!

Contents

Chapter 1

Introduction

Synchronization is ubiquitous. The human sleep-wake cycle synchronizes to the rising and setting of the sun, leading to a wave of alarm clocks going off at nearly the same time every morning. After getting up, some of those people will hop on a treadmill or hit the road and go for a run, which is only possible if their limbs operate in a synchronized fashion. Later, as they commute to work, some of those people will enjoy the synchronized rhythms and frequencies of the music coming from their radios. Some of that music may come from a CD, which utilizes the synchronized light from a laser in order to read the contents of the disc.

If this hypothetical day were on June 10, 2000, some of those people may have tuned into the nightly news to see crowds of pedestrians walking across the newly opened London Millennium Footbridge in lock-step [1]. The bridge's unexpected behavior led to its closure for nearly two years. The work that I present here focuses on synchronization of this sort: spontaneous synchronization of many similar phase oscillators.

To make the problems tractable, while still being applicable to real-world systems, I have focused my attention on the synchronization of phase oscillators. A phase oscillator is a system described by a single degree of freedom: its phase. The gait of an individual is periodic and unless the person changes gait from a walk to a run, the amplitude of the gait is relatively constant. Another example of a phase oscillator is a ball tied to the end of a string being swung in a circle. If the length of the string is fixed, the ball's motion can be described simply in terms of the angular phase of the ball. Replacing the string with a spring would lead to an oscillator with two degrees of freedom: the distance of the ball from the center of rotation and the angular phase of the ball. Others have considered even more complex

systems, such as the synchronization of chaotic oscillators. However, in many systems that exhibit synchronization, the dynamics of individual elements can be well approximated by phase oscillators, giving a simple model that still exhibits fascinating collective behavior.

Although I could focus on the synchronization of two oscillators, I chose to study the collective phenomena found in large systems. Experiments on the Millennium Bridge found that large amplitude oscillations in the bridge and synchronous walking only arose when more than 160 people walked across it at the same time [2]. The smallest population I consider is the collection of 16 motors in the experimental work that makes up the second half of this thesis, but in simulations I consider the behavior of anywhere from 100 to 100,000 oscillators. Analytical treatments for more than a few interacting oscillators become intractable unless the system under consideration is large enough to make statements about collective behavior.

Human walking rates vary, as do the natural speeds of the motors in my experiments. Therefore, I concentrate on systems of interacting oscillators that are similar but not identical. The differential equations describing the dynamics of each oscillator match, differing only in oscillator-specific parameters such as the oscillator's natural velocity. Some people naturally walk with faster or slower gaits than others. The only disorder in the systems I study comes from the disorder in the natural speeds (as well as the initial positions, which are usually randomized), and in particular I do not consider the effects of adding noise to the system [3]. In short, the disorder in my systems is quenched.

Just as the effect of one person's footfall on the Millennium Bridge transmitted forces to every other person on the bridge, I consider oscillators whose coupling is global in one sense or another. Many have considered systems with local coupling and discovered interesting behavior. Systems with circular boundary conditions and finite-range coupling exhibit a partially-entrained state dubbed the 'chimera' state [4, 5, 6, 7, 2]. Two-dimensional systems on a lattice give rise to vortices [8]. Local coupling leads to fascinating behavior that may apply tangentially to some of the work I present here, but I focus on global coupling.

Populations of coupled phase oscillators of the sort I have described were first studied by

Winfree [9], who considered a very general model with the form

$$\dot{\theta}_i = \omega_i + \frac{K}{N} \sum_{j=1}^{N} P(\theta_j) R(\theta_i). \tag{1.1}$$

The function $P(\theta_j)$ represents an oscillator's phase-dependent influence on other oscillators while $R(\theta_i)$ represents an oscillator's phase-dependent sensitivity to other oscillators' influence. The specific forms for P and R are unspecified and the magnitude of K governs the strength of the coupling between the oscillators. Using purely geometric arguments, Winfree argued that populations of oscillators coupled as described synchronize only when K exceeds some (typically nonzero) threshold value.

Winfree's pioneering work came first, but the canonical model for coupled phase oscillators is the Kuramoto model [10]. Kuramoto refined Winfree's work by restricting his model to a very specific form for the coupling between the oscillators—the sine of the difference of the phases:

$$\dot{\theta}_i = \omega_i + \frac{K}{N} \sum_{j=1}^{N} \sin(\theta_j - \theta_i). \tag{1.2}$$

The oscillators are generally attracted to each other: an oscillator lagging behind another gets a boost since $\theta_j - \theta_i > 0$, whereas an oscillator leading another gets pulled back since $\theta_j - \theta_i < 0$. The specific form of the coupling makes Kuramoto's model far less general than Winfree's,[1] but surprisingly well suited to analytic treatment. Whereas Winfree used geometric arguments to show that a transition occurred at nonzero coupling, Kuramoto was able to explicitly calculate the strength of the critical coupling. Because important characteristics can be obtained analytically, the Kuramoto model provides an analytical framework for generalizations.

The Kuramoto model is a mean field model. To see this, consider the following trick. Define the quantity

$$r\, e^{\imath \psi} \equiv \frac{1}{N} \sum_{j=1}^{N} e^{\imath \theta_j}. \tag{1.3}$$

[1] It might be tempting to think of Kuramoto's model as representing the first term in a Fourier series expansion of $P(\theta_j) R(\theta_i)$. However, Crawford [11] showed that additional harmonics lead to very different behavior, which unfortunately limits the scope of applicability of the Kuramoto model.

This quantity can be interpreted as the phasor average of all the oscillators and using it I can rewrite Kuramoto's model:

$$\dot{\theta}_i = \omega_i + K\,\Im\left\{\frac{1}{N}\sum_{j=1}^{N} e^{\imath\,\theta_j - \imath\,\theta_i}\right\} \tag{1.4}$$

$$= \omega_i + K\,\Im\left\{e^{-\imath\,\theta_i}\frac{1}{N}\sum_{j=1}^{N} e^{\imath\,\theta_j}\right\} \tag{1.5}$$

$$= \omega_i + K\,\Im\left\{e^{-\imath\,\theta_i} r\,e^{\imath\,\psi}\right\} \tag{1.6}$$

$$= \omega_i + r\,K\sin\left(\psi - \theta_i\right). \tag{1.7}$$

Each oscillator interacts exclusively with the phasor average, making it a mean field. Furthermore, the coupling has the same form as the pairwise coupling: oscillators that lead (lag) the mean field are slowed-down (sped-up) relative to their natural speeds. Put differently, synchronized oscillators whose natural speeds are slower (faster) than the synchronized speed typically lag (lead) the mean field.

Kuramoto's model undergoes a phase transition, as predicted by Winfree, and characteristics of the transition can be solved explicitly in the large-N limit. The phasor average serves not only as a mean field but also as an order parameter for the model. If the natural speeds ω_i are sampled from a Lorentzian distribution with full-width-half-maximum γ, the order parameter has the following form:

$$r = \begin{cases} \sqrt{1 - \frac{K_c}{K}} & K > K_c = 2\gamma \\ 0 & K < K_c \end{cases} \tag{1.8}$$

Other symmetric unimodal velocity distributions show similar behavior, though the critical value of the coupling K_c depends upon the distribution $g(\omega)$ as

$$K_c = \frac{2}{\pi\,g(0)}. \tag{1.9}$$

(Note that I will use $g(\omega)$ throughout the first part of this dissertation to denote the distribution from which I sample the oscillator speeds.) For a Lorentzian distribution $K_c = 2\gamma$,

and for a Gaussian distribution, $K_c \approx 1.5957\,\sigma$. Kuramoto derived a closed expression for $r\,(K)$ for a Lorentzian distribution; the Lorentzian distribution was the only one for which closed expressions were obtained until the recent work of Ott and Antonsen [12].

The Kuramoto model serves as the theoretical and conceptual backdrop for this dissertation, which is split into two parts. The first part, Chapters two and three, detail my theoretical and numerical work exploring finite-size effects in the Kuramoto model. The second part, Chapters four and five, detail my experimental observations and modeling of a laboratory system that exhibits synchronization. The model that I develop in Chapter five shows that only a slight extension to the Kuramoto model leads to predictions that closely match the experimental measurements.

The Kuramoto model—the canonical model for spontaneous synchronization of many interacting phase oscillators—is over 30 years old. However, many aspects of and extensions to that model remain unexplored. In the remainder of this dissertation, I will explain the contributions I have made to this field.

Part I

The Finite Kuramoto Model

Introduction to the First Part

In contrast to the second part, in which I focus on my experimental findings, this first part of the dissertation covers my numerical and theoretical work on the Kuramoto model. In Chapter 2 I develop and analyze a complicated numerical scheme for predicting the behavior of the Kuramoto model based on the assumption that the order parameter r is approximately constant and rotates at a constant rate Ω. The predictions work very well for population-specific predictions, either agreeing with high accuracy or failing in an easily identified way. In Chapter 3, I interpret the discontinuities predicted by the numerical scheme as avalanches and analyze the scaling behavior of the avalanches, comparing the results with other finite-size results for the Kuramoto model and for the Ising model.

Chapter 2

Self-consistent Scheme

The Kuramoto model, which I introduced already, is this:

$$\dot{\theta}_i = \omega_i + r\,K \sin\left(\psi - \theta_i\right), \qquad\qquad r\,e^{\imath\,\psi} \equiv \frac{1}{N}\sum_{j=1}^{N} e^{\imath\,\theta_j}. \tag{2.1}$$

I sample the speeds of the oscillators ω_i from a normalized distribution $g\left(\omega\right)$, which satisfies

$$g\left(\omega\right) > 0 \qquad \forall\omega \tag{2.2}$$

$$\int_{-\infty}^{\infty} g\left(\omega\right) = 1 \tag{2.3}$$

The classical analysis of the Kuramoto model typically follows these steps: (1) assume that $g\left(\omega\right)$ is unimodal and symmetric, such as a Gaussian or a Lorentzian distribution. Next, note that the degree of synchronization should depend on the details of the distribution of the speeds of the oscillators, but not the average oscillator speed. In other words, if I shift the mean of the distribution of the oscillators $g\left(\omega\right) \to g\left(\omega - \hat{\omega}\right)$, the *speed* of the synchronized state ω_s may change to $\omega_s + \hat{\omega}$, but the *degree* of the synchronization will not. As such, (2) assume the distribution is centered at zero. (Assumptions 1 and 2 together imply that $g\left(\omega\right)$ is an even function.) When the system becomes synchronized (i.e., $K > K_c$), the degree of synchronization will exhibit fluctuations that scale inversely with the population size. In the asymptotic limit $N \to \infty$, the fluctuations become negligible. As such, (3) assume the magnitude of r is constant. Since the large-N limit applies, (4) replace sums over the population with integrals over probability distributions. With a fair amount of mathematics that I will not detail here [13], all of this leads to the following implicit expression for the order parameter r:

$$r = r\,K \int_{-\pi/2}^{\pi/2} \cos^2\theta \cdot g\left(r\,K\,\sin\theta\right) d\theta. \tag{2.4}$$

Many illuminating results can be drawn from equation 2.4, the most important of which is the phase transition already discussed.

Only the second step in the classical analysis of the Kuramoto model is general. The first, third, and fourth steps are approximations. The combination of the first and fourth assumptions in particular makes equation 2.4 unsuitable for studying finite-size effects since finite samplings have no guarantee of even sampling and probability distributions can smear finite-size effects. Simulations of the Kuramoto model for finite population size [specific, finite samplings from $g(\omega)$] show considerable variation across populations. By assuming that all samplings from $g(\omega)$ behave the same, equation 2.4 ignores the effects of finite sampling.

In the coming sections I motivate and then explain an analysis that parallels the classical analysis of the Kuramoto model but which does not completely suppress finite-size effects. The literature contains variations on this analysis. My contribution differs from previous work by giving full consideration to the unentrained oscillators, including a proper interpretation of the resulting imaginary contributions to the order parameter, and by making a detailed comparison between the predictions and numerical simulations.

2.1 Direct Numerical Simulations

Useful theory must make testable predictions. Before delving into the theory, I first introduce the numerical methods I use to test my predictions and the techniques I utilize to visualize the behavior of the Kuramoto system. I compactly visualize my simulation results by constructing color density plots; the simulations themselves are a CUDA implementation of a fourth-order Runge-Kutta method to perform direct numerical simulations of equation 2.1 on populations of $N = 512$ oscillators. The variation in behavior of four distinct populations—four samplings from the same underlying Gaussian distribution—demonstrate that the classical analysis has room for improvement.

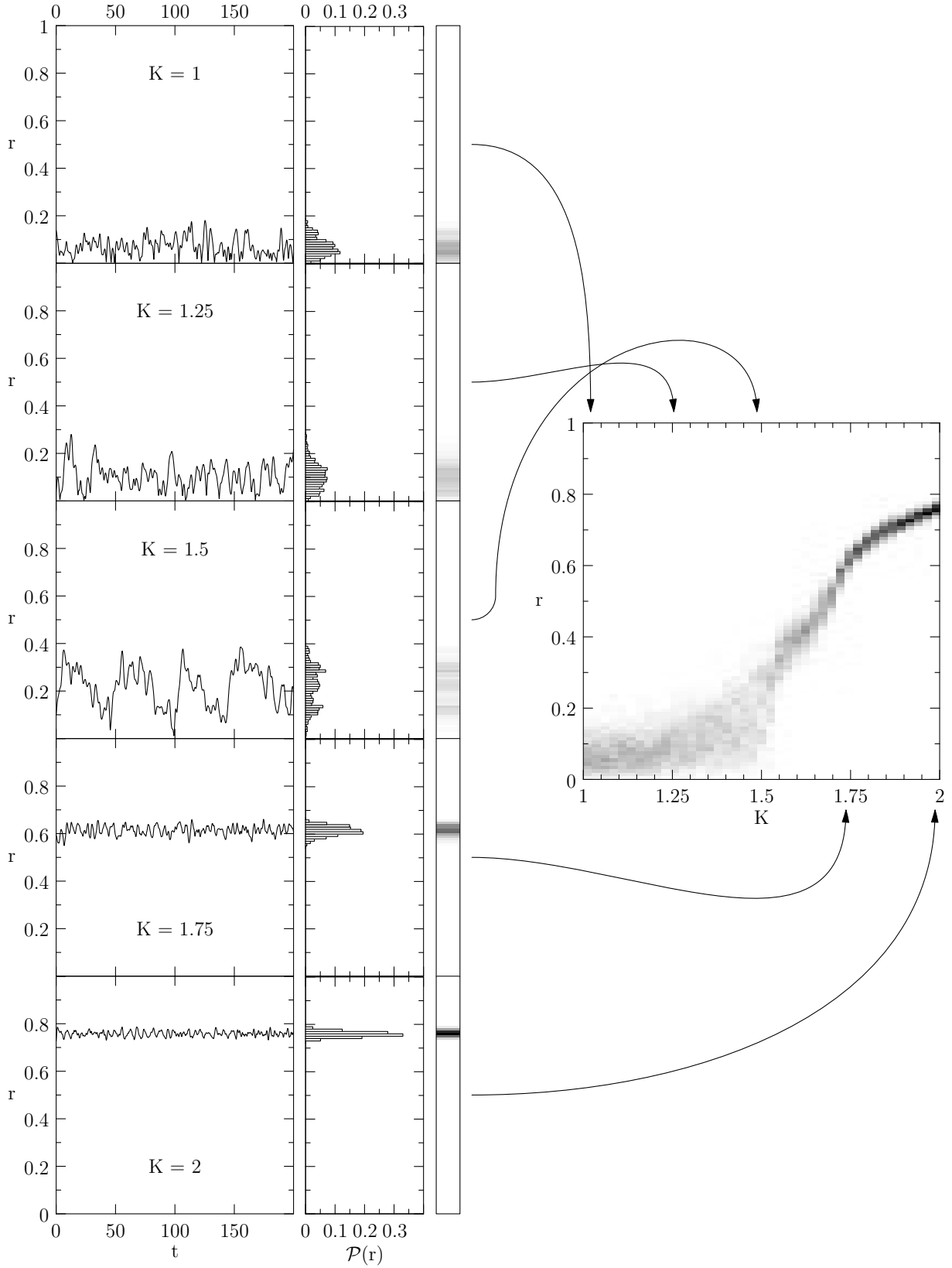

Figure 2.1: The method for building color density plots. Histograms are created from time series of r(t) for fixed K. The histograms are normalized, making them probability distributions, and displayed consecutively as gray-scale columns in the color density plot.

Throughout this dissertation I make regular use of color density plots, though they represent slightly different information in each of the two Parts. Figure 2.1 depicts how I create such plots for the Kuramoto simulations. For a given population, I set random initial positions and run the system for a transient period at a low coupling. I take a lengthy measurement of $r\,(t)$ at that coupling, increase the coupling slightly, and let the system run for another transient period before measuring again. By repeating this procedure for many values of K, I build up a collection of time series $\{r_i,\, t_i\}_K$. Ignoring the time dependence, I examine the set $\{r_i\}_K$ and construct the probability distributions $\mathcal{P}\,(r|K)$. Displaying each of these distributions as gray-scale columns and laying them out sequentially leads to the full color density plot. Although I describe a direction-dependent process (slowly increasing K), performing the simulation in the other direction nearly always gives the same behavior within the K-resolution of the numerics. I have not observed meaningful differences between directions for any simulation of $N = 512$ oscillators.

Figure 2.2 shows the behavior of four different populations with speeds sampled from a centered Gaussian distribution

$$g_0\,(\omega) = \frac{1}{\sqrt{2\,\pi\,\sigma^2}} e^{-\frac{(\omega-\bar{\omega})^2}{2\,\sigma^2}} \tag{2.5}$$

with width $\sigma = 1\,rad/s$. For each population, a histogram indicates the actual distribution of the natural speeds $g_a\,(\omega)$, $g_b\,(\omega)$, etc., in contrast to the original Gaussian $g_0\,(\omega)$. I constructed populations (a) and (b) so that for each oscillator ω_i, the population contains another oscillator $\omega_j = -\omega_i$. For this reason, I call populations (a) and (b) *symmetric*, and populations (c) and (d) *unsymmetric*. The accompanying r vs K color density plots show the behavior of the direct numerical simulations. I run these simulations by starting at low coupling and with the oscillators in random initial positions, then slowly increasing the coupling as already described. For the symmetric populations, I tried both symmetric and unsymmetric initial conditions and the results do not show any observable difference. Each of the simulations cover 501 K-values from 1.2 to 2.0 and 400 r-values ranging from 0 to 1. The transient for each K value lasted 1000s, and the measurement period lasted 20,000s.

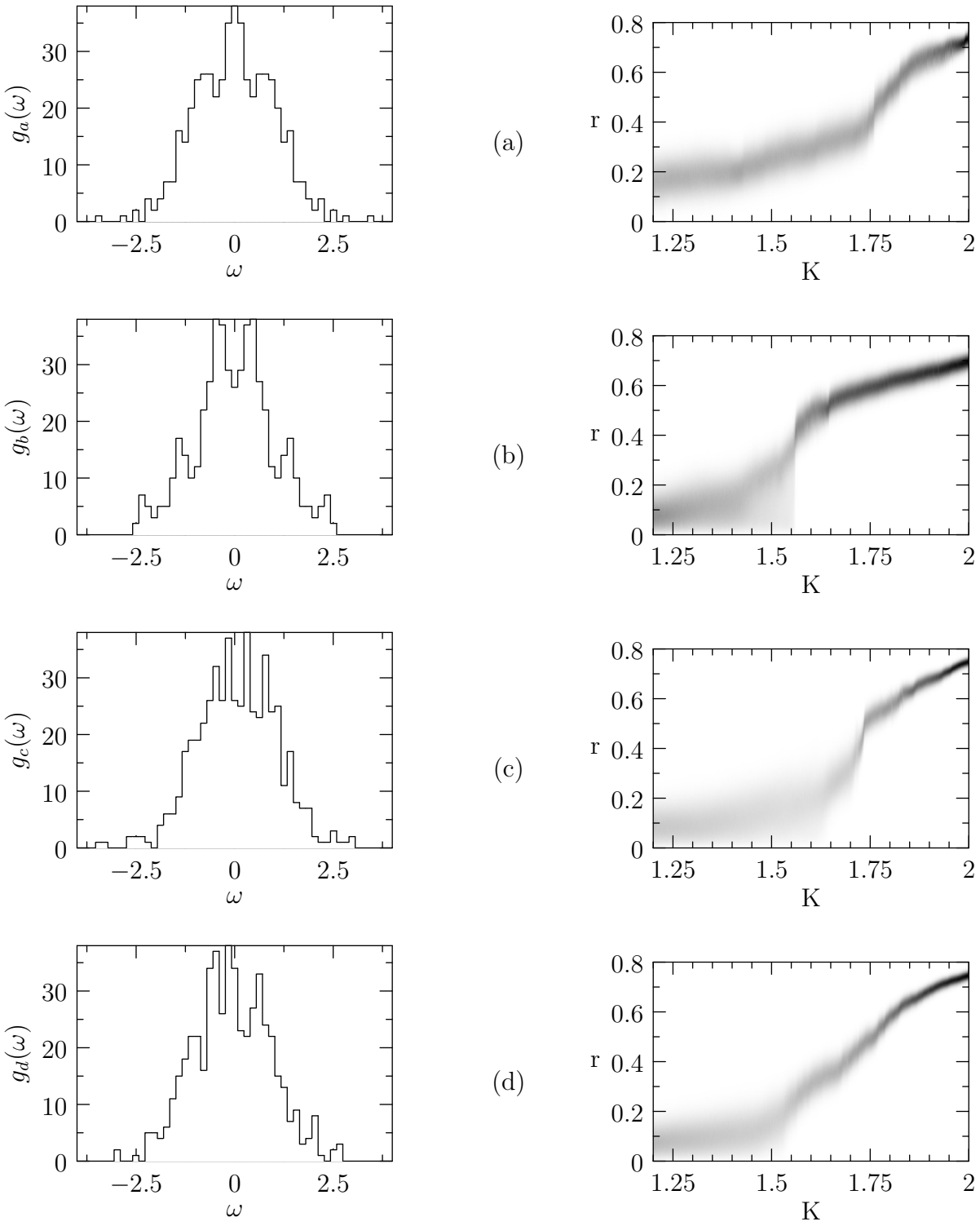

Figure 2.2: Four examples illustrating the range of behaviors possible for identically sized samplings of the same distribution $g_0(\omega)$ (in this case, a Gaussian distribution). For these and all other figures in this Chapter, $N = 512$.

To perform the time-stepping, I use a fourth-order Runge-Kutta method implemented in CUDA, with time steps of $\Delta t = 0.125$s.

Although the behavior of all four populations in figure 2.2 show substantial upward trends in the vicinity of the critical coupling $K_c = 1.6$, they also exhibit a wide variety of behavior, in spite of having the same parent distribution $g_0(\omega)$. Populations (b) and (c) exhibit substantial jumps in the degree of synchronization whereas populations (a) and (d) are comparatively smooth. Furthermore, the K value for the jumps in populations (b) and (c) do not agree, and population (c) does not show the curtain-like effect found in population (b) below $K = 1.55$. The specific populations agree in the basics but disagree in the specifics. The remainder of this Chapter details my work at predicting these specifics.

2.2 Approximation of Average Mean Field

The order parameter for a finite-sized population fluctuates, but for most values of K the order parameter appears to have a well-defined average. I will take this as my starting point: that r is well approximated by a constant value, and that it rotates at a constant rate Ω.

For reasons that will hopefully become clear over the course of the discussion, I will keep the definition of r in equation 2.1 but I will work with Sakaguchi's generalization of Kuramoto's model [14]:

$$\dot{\theta}_j = \omega_j + r\,K \sin(\psi - \theta_j - \alpha)\,. \tag{2.6}$$

Adding the phase offset α has two effects: it decreases the degree of synchronization for a given population and value of K, and it causes the synchronized velocities to become skewed. To get results particular to Kuramoto's model I need only set the phase offset α to zero. Furthermore, I will consider the dynamics that describe how each oscillator varies from the mean field, $\Delta\theta_i \equiv \theta_i - \psi - \alpha$:

$$\Delta\dot{\theta}_i = \omega_i - \dot{\psi} + r\,K \sin(\psi - \Delta\theta_i - \psi + \alpha - \alpha) \tag{2.7}$$

$$= \omega_i - \dot{\psi} - r\,K \sin(\Delta\theta_i)\,. \tag{2.8}$$

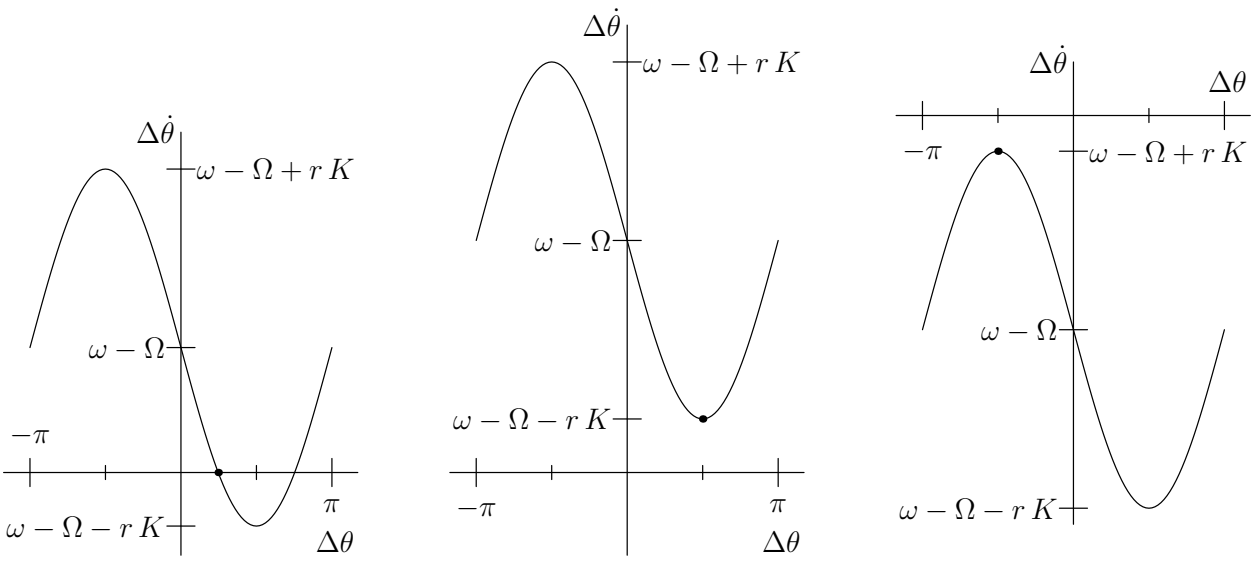

Figure 2.3: A phase portrait for an individual oscillator with natural speed ω interacting with a mean field of magnitude r and a speed Ω. (In these figures I set α to 0.) If $|\omega - \Omega| < r\,K$, as in (a), the oscillator has a stable fixed point with respect to the mean field as marked by the dot. If $\Omega + r\,K < \omega$, as in (b), or $\omega < \Omega - r\,K$, as in (c), the oscillator always moves with respect to the mean field, but it slows down when it is $\pi/2$ out of phase with the field. The slowest points for both of these scenarios are marked with dots. The subfigures correspond to an entrained oscillator (a), a fast oscillator (b), and a slow oscillator (c).

By assuming that r is approximately constant and $\dot{\psi} \approx \Omega$, the dynamics for $\Delta\theta_i$ reduce to a set of uncoupled Adler equations [15] that depend only on the position of oscillator i:

$$\Delta\dot{\theta}_i = \omega_i - \Omega - r\,K \sin\left(\Delta\theta_i\right). \tag{2.9}$$

The phase portrait for the dynamics of $\Delta\theta_i$ indicates that all oscillators with natural speeds that satisfy $-r\,K < \omega_i - \Omega < r\,K$ approach a stable fixed point $\Delta\theta_i$:

$$\sin\Delta\theta_i = \frac{\omega_i - \Omega}{r\,K}, \tag{2.10}$$

marked in figure 2.3(a) by a dot. (The other zero in figure 2.3(a) is a fixed point, but it is unstable.) Oscillators whose natural speeds fall outside the range of stable speeds, i.e. $r\,K < |\omega_i - \Omega|$, do not synchronize but have phase-dependent speeds. The dots in figures 2.3(b)-(c) mark the phases corresponding with the slowest relative velocities, i.e. the

positions where unentrained oscillators spend most of their time and are most likely to be found.

Having obtained predictions for the positions of entrained oscillators and speeds for unentrained oscillators, the question naturally arises: is this distribution of positions consistent with the assumed value of r? The definition for r and ψ was given as

$$r\,e^{\imath\,\psi} \equiv \frac{1}{N}\sum_{j=1}^{N} e^{\imath\,\theta_j} \tag{2.11}$$

which I can rewrite in terms of the $\Delta\theta_i$ as

$$r\,e^{\imath\,\psi} = \frac{1}{N}\sum_{j=1}^{N} e^{\imath\,\Delta\theta_j + \imath\,\psi + \imath\,\alpha} \tag{2.12}$$

$$\implies r\,e^{-\imath\,\alpha} = \frac{1}{N}\sum_{j=1}^{N} e^{\imath\,\Delta\theta_j}. \tag{2.13}$$

I have assumed r is constant, but the unentrained oscillators will contribute to this sum in a time-dependent way. What I really want is the average contribution of each oscillator. To assist in the notation, I will use Θ_e to designate the set of entrained oscillators and Θ_u the set of unentrained oscillators. In that case,

$$r\,e^{-\imath\,\alpha} = \frac{1}{N}\sum_{\theta_j\in\Theta_e} e^{\imath\,\Delta\theta_j} + \frac{1}{N}\sum_{\theta_j\in\Theta_u} \left\langle e^{\imath\,\Delta\theta_j}\right\rangle \tag{2.14}$$

where angle-brackets denote long-time averages. Since the entrained oscillators have fixed positions, the first sum is easy to compute:

$$\sum_{\theta_j\in\Theta_e} e^{\imath\,\Delta\theta_j} = \sum_{\theta_j\in\Theta_e} (\cos\Delta\theta_j + \imath\sin\Delta\theta_j) \tag{2.15}$$

$$= \sum_{\theta_j\in\Theta_e} \sqrt{1 - \frac{(\omega_j-\Omega)^2}{r^2K^2}} + \imath\sum_j \frac{\omega_j-\Omega}{r\,K}. \tag{2.16}$$

In taking the large-N limit, the classical analysis assumes $\Omega = \bar{\omega}$ and neglects the imaginary terms (as well as the contributions from the unentrained oscillators) under the assumption that they are negligible. For symmetric populations, that assumption is valid: the

imaginary terms exactly cancel, leading to the prediction

$$r_{sym} = \frac{1}{N} \sum_{\theta_j \in \Theta_e} \sqrt{1 - \frac{(\omega_j - \bar{\omega})^2}{r^2 K^2}}. \tag{2.17}$$

In other words, if I discard the imaginary term in my expression, I have a population-specific prediction for the order parameter. Before attempting the complicated calculations involved in determining the contributions of the unentrained oscillators, I ought to examine how well the current expression performs, both for symmetric as well as unsymmetric populations. Figure 2.4 shows that for symmetric populations (a) and (b) the predictions either agree very well or fail miserably, and the failures correspond to deep turn-arounds in the prediction. Put differently, the failures are *easy to identify* from the predictions themselves, even without the help of numerical simulations. Furthermore, the failures correspond to important changes in the simulation's behavior. This gives me a tool to predict what the system will do generally as well as where to look for interesting behavior.

Predictions for unsymmetric populations also show impressive agreement and impressive failure, but fluctuate more substantially and fail more randomly than they do for the symmetric populations. The failures for the unsymmetric populations are difficult—if not impossible—to identify from the predictions alone. For example, in population (c) the numerics exhibit a rapid change near $K = 1.72$, but the scheme predicts a continuous drop closer to $K = 1.75$. Unlike the failure for population (b), the scheme's predictions for population (c) do not give any hint that they might fail. For population (d), the scheme's predictions for $K > 1.75$ deviates substantially more from the numerical mean than for the evenly sampled populations and the substantial failure near $K = 1.7$ does not correspond to any substantial change in behavior of the numerics.

Given the complicated fluctuations in some of the time series shown in figure 2.1 (the time series at $K = 1.5$ is not atypical), the simple numerical scheme performs quite well for symmetric populations. Can a similar approach improve the predictions for the unsymmetric populations? To answer that question, I calculate the average contributions that the

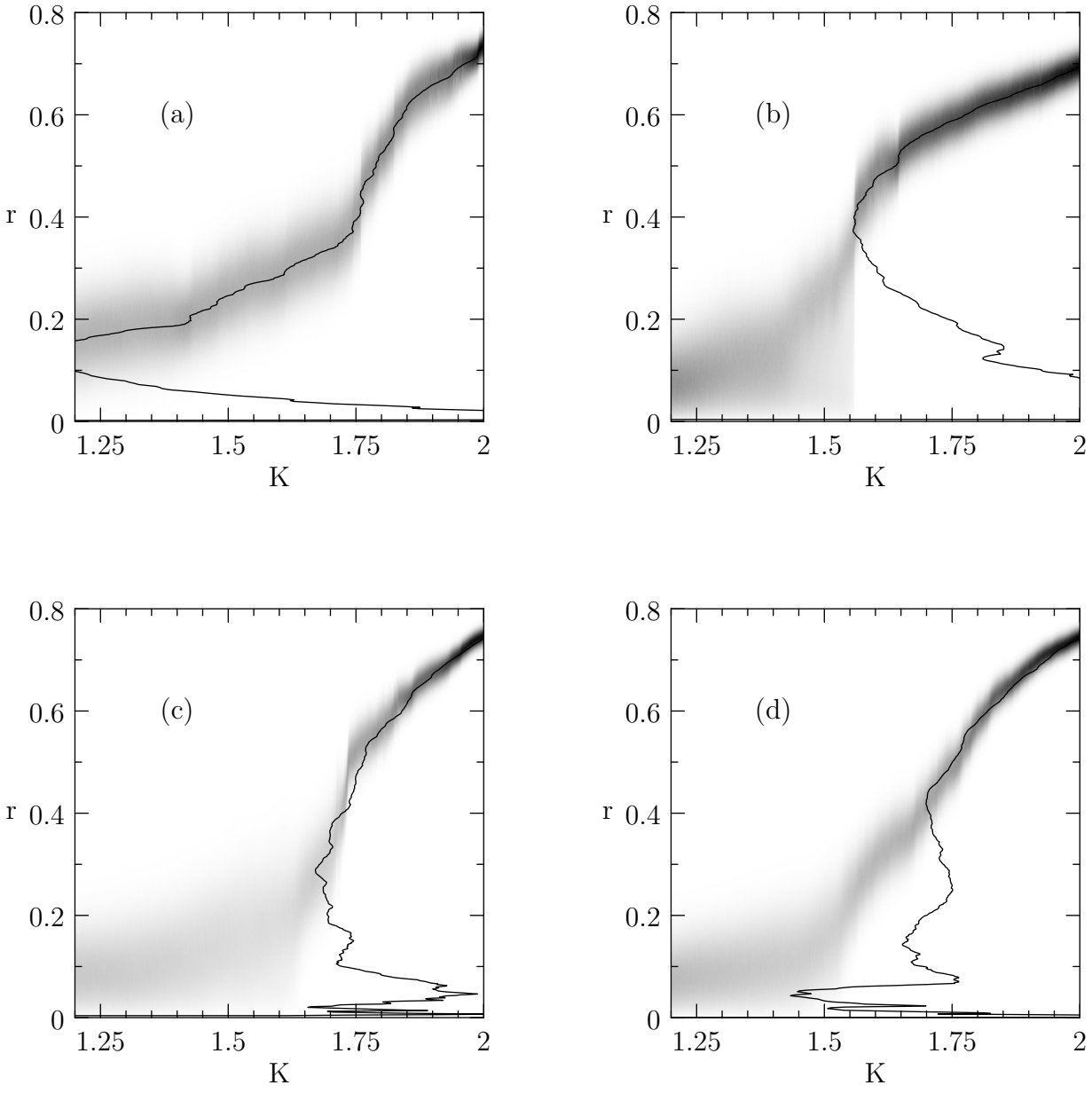

Figure 2.4: Simulations and predictions of the order parameter for the populations shown in figure 2.2. The agreement between the predictions and the numerics for figures (a) and (b) are very good; these populations are symmetric. The agreement for figures (c) and (d), unsymmetric populations, are not as good.

unentrained oscillators make to the order parameter prediction in the next section.

2.3 Unentrained Contributions

The unentrained oscillators do not have fixed positions with respect to the mean field, but their speeds depend on their position with respect to the mean field's phase according to equation 2.9. Because the unentrained oscillators move constantly, and because they never back-track with respect to the mean-field, the likelihood of finding any one of them at a given phase (relative to the mean field) is simply proportional to that oscillator's relative velocity:

$$\mathcal{P}_i\left(\Delta\theta\right) = \frac{C_i}{\omega_i - \Omega - r\,K\sin\left(\Delta\theta\right)}. \tag{2.18}$$

$\mathcal{P}_i\left(\Delta\theta\right)$ is not uniform and as I will soon show, this leads to imaginary contributions to the self-consistent estimate for the order parameter.

The normalization constant C_i must satisfy the standard normalization condition for probability distributions:[1]

$$1 = \int_{-\pi}^{\pi} \mathcal{P}_i\left(\theta\right) d\theta, \tag{2.19}$$

$$= C_i \int_{-\pi}^{\pi} \frac{d\theta}{\omega_i - \Omega - r\,K\sin\left(\theta\right)}. \tag{2.20}$$

To evaluate this integral, I transform it into a contour integral about the unit circle. Taking $z \equiv e^{\imath\,\theta}$, in which case $d\theta = dz/\imath z$, I have

$$C_i^{-1} = \oint \frac{dz/\imath z}{\omega_i - \Omega - r\,K\left(z - z^{-1}\right)/2\imath} \tag{2.21}$$

$$= \frac{-2}{r\,K} \oint \frac{dz}{z^2 - 2\imath\frac{\omega_i - \Omega}{r\,K}\,z - 1}. \tag{2.22}$$

The quadratic expression in the denominator has two roots

$$z_i^{\pm} = \imath\frac{\omega_i - \Omega}{r\,K} \pm \sqrt{1 - \frac{\left(\omega_i - \Omega\right)^2}{r^2K^2}}. \tag{2.23}$$

[1]Note that as defined, the sign of C_i ensures that the probability is strictly positive, as required for a properly defined probability.

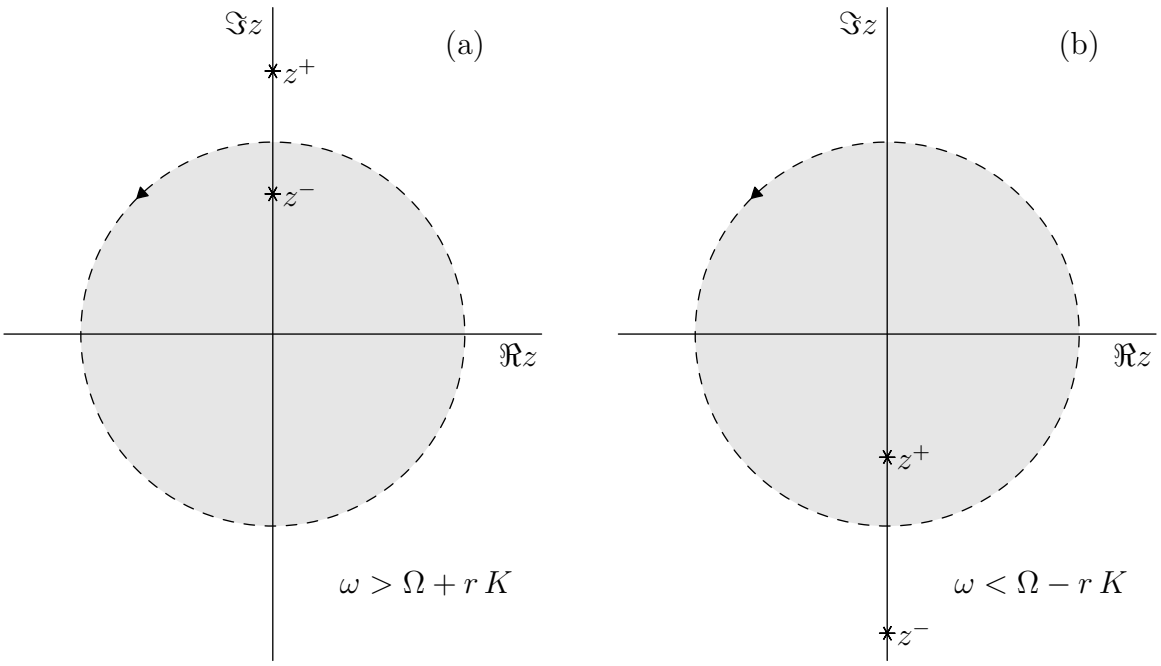

Figure 2.5: The pole structure for equation 2.22 (or more simply equation 2.25). The pole that contributes to the integral depends on whether the oscillator's natural speed is much faster (a) or much slower (b) than the synchronized speed. The values of $z^{\pm}$ are given in equation 2.24.

By construction, $|\omega_i - \Omega| > r\,K$, which means the square-root term is imaginary, so I write the roots as

$$z_i^{\pm} = \imath \frac{\omega_i - \Omega}{r\,K} \pm \imath \sqrt{\frac{(\omega_i - \Omega)^2}{r^2 K^2} - 1}. \tag{2.24}$$

Both of these roots are purely imaginary and have the form $x \pm \sqrt{x^2 - 1}$ with $x^2 > 1$. Whether x is positive or negative, one of the two roots has a magnitude greater than 1 while the other has a magnitude less than one. For example, if $\omega_i - \Omega$ is positive then $\Im\left\{z_i^+\right\} > 1$ and $0 < \Im\left\{z_i^-\right\} < 1$, as depicted in figure 2.5(a). The contour integral can be written in much simpler terms as

$$C_i^{-1} = \frac{-2}{r\,K} \oint \frac{dz}{\left(z - z_i^+\right)\left(z - z_i^-\right)} \tag{2.25}$$

and only one of the two roots contributes to the integral. Again considering $\omega_i - \Omega > 0$, z_i^-

is the applicable pole and the contour integral evaluates to

$$C_i^{-1} = \frac{-2}{r\,K} \cdot 2\pi\imath \cdot \frac{1}{z_i^- - z_i^+} \qquad \text{for } \omega_i - \Omega > 0 \tag{2.26}$$

$$= \pi \frac{-4\imath}{r\,K} \frac{1}{-2\imath\sqrt{\frac{(\omega_i-\Omega)^2}{r^2K^2} - 1}} \qquad \text{for } \omega_i - \Omega > 0 \tag{2.27}$$

$$= \frac{2\,\pi}{\sqrt{(\omega_i - \Omega)^2 - r^2K^2}} \qquad \text{for } \omega_i - \Omega > 0, \tag{2.28}$$

giving a normalization constant of

$$C_i = \sqrt{(\omega_i - \Omega)^2 - r^2K^2}/2\pi \qquad \text{for } \omega_i - \Omega > 0. \tag{2.29}$$

For $\omega_i - \Omega < 0$, z_i^+ is the applicable pole and C_i has the opposite sign, giving a general expression for C_i as

$$C_i = \frac{\omega_i - \Omega}{2\,\pi}\sqrt{1 - \frac{r^2K^2}{(\omega_i - \Omega)^2}}. \tag{2.30}$$

Computing the contribution of this oscillator to the order parameter is equally laborious (but thankfully no harder). The integral and its associated contour integral for that contribution is

$$\left\langle e^{\imath\,\Delta\theta_i} \right\rangle = \frac{\omega_i - \Omega}{2\,\pi}\sqrt{1 - \frac{r^2K^2}{(\omega_i - \Omega)^2}} \int_{-\pi}^{\pi} \frac{e^{\imath\,\theta} d\theta}{\omega_i - \Omega - r\,K\sin\theta} \tag{2.31}$$

$$= \frac{\omega_i - \Omega}{2\,\pi}\sqrt{1 - \frac{r^2K^2}{(\omega_i - \Omega)^2}} \cdot \frac{-2}{r\,K} \oint \frac{z\,dz}{z^2 - 2\imath\frac{\omega_i-\Omega}{r\,K}\,z - 1}. \tag{2.32}$$

The denominator of the associated contour integral is the same, leading to the same poles in the evaluation of the contour. The end result of all of the calculations is

$$\left\langle e^{\imath\,\Delta\theta_i} \right\rangle = \imath\frac{\omega_i - \Omega}{r\,K} - \imath\,(\omega_i - \Omega)\sqrt{\frac{1}{r^2K^2} - \frac{1}{(\omega_i - \Omega)^2}}. \tag{2.33}$$

Contributions from an unentrained oscillator are astonishingly similar to contributions

from an entrained oscillator. Here are the three different contributions, for comparison:

$$\left\langle e^{\imath\,\Delta\theta_i} \right\rangle = \imath\frac{\omega_i - \Omega}{r\,K} - \sqrt{1 - \frac{(\omega_i - \Omega)^2}{r^2K^2}} \qquad \text{for } \omega_i - \Omega > r\,K, \tag{2.34}$$

$$\left\langle e^{\imath\,\Delta\theta_i} \right\rangle = \imath\frac{\omega_i - \Omega}{r\,K} + \sqrt{1 - \frac{(\omega_i - \Omega)^2}{r^2K^2}} \qquad \text{for entrained oscillators,} \tag{2.35}$$

$$\left\langle e^{\imath\,\Delta\theta_i} \right\rangle = \imath\frac{\omega_i - \Omega}{r\,K} + \sqrt{1 - \frac{(\omega_i - \Omega)^2}{r^2K^2}} \qquad \text{for } \omega_i - \Omega < -r\,K. \tag{2.36}$$

The only real components arise from entrained oscillators (the square-root terms for the unentrained oscillators yield imaginary contributions). The sign of the square-root terms for the unentrained oscillators function in such a way that as ω_i gets farther from Ω, the (imaginary) contribution approaches zero. As mentioned in the previous section, the imaginary terms exactly cancel for symmetric samplings, whereas the real terms sum.

Having determined the average contribution that an unentrained oscillator makes, I next assemble and analyze the predictions of the order parameter, properly accounting for all oscillators.

2.4 The full scheme

Combining the contributions from the entrained as well as the unentrained oscillators gives the self-consistent scheme for the mean-field r:

$$\begin{aligned} r\,e^{-\imath\,\alpha} = &\sum_{\theta_i \in \Theta_e} \sqrt{1 - \frac{(\omega_i - \Omega)^2}{r^2K^2}} \\ &+ \imath \sum_{i=1}^{N} \frac{\omega_i - \Omega}{r\,K} - \imath \sum_{\theta_i \in \Theta_u} (\omega_i - \Omega) \sqrt{\frac{1}{r^2K^2} - \frac{1}{(\omega_i - \Omega)^2}}. \end{aligned} \tag{2.37}$$

How does this compare this result with previous predictions and how do I interpret this equation?

In order to compare the predictions of the full scheme in equation 2.37 to the predictions for the large-N limit, I first rewrite the scheme in the large-N limit as a collection of integrals:

$$
\begin{aligned}
r\,(\Omega,\,K)\;e^{-\imath\,\alpha} = & \int_{\Omega-r\,K}^{\Omega+r\,K} \sqrt{1-\frac{(\omega-\Omega)^2}{r^2K^2}}\,g\,(\omega)\,d\omega \\
& + \imath \int_{-\infty}^{\infty} \frac{\omega-\Omega}{r\,K}\,g\,(\omega)\,d\omega \\
& - \imath \int_{-\infty}^{\Omega-r\,K} (\omega-\Omega)\,\sqrt{\frac{1}{r^2K^2}-\frac{1}{(\omega-\Omega)^2}}\,g\,(\omega)\,d\omega \\
& - \imath \int_{\Omega+r\,K}^{\infty} (\omega-\Omega)\,\sqrt{\frac{1}{r^2K^2}-\frac{1}{(\omega-\Omega)^2}}\,g\,(\omega)\,d\omega
\end{aligned}
\tag{2.38}
$$

If I consider an even distribution $g\,(\omega)$ centered at zero (which means $\Omega = 0$), the imaginary terms vanish, leaving

$$
r\,e^{-\imath\,\alpha} = \int_{-r\,K}^{r\,K} \sqrt{1-\frac{\omega^2}{r^2K^2}}\,g\,(\omega)\,d\omega. \tag{2.39}
$$

Because the imaginary sums have vanished, $\alpha = 0$. A simple trigonometric substitution leads to the expressions

$$
\sin\phi = \frac{\omega}{r\,K}, \qquad\qquad d\omega = r\,K\cos\phi d\phi, \tag{2.40}
$$

which allow me to rewrite the expression for r as

$$
r = \int_{-\pi/2}^{\pi/2} \cos\phi\cdot g\,(r\,K\sin\phi)\,r\,K\cos\phi\,d\phi \tag{2.41}
$$

$$
= r\,K\int_{-\pi/2}^{\pi/2} \cos^2\phi\cdot g\,(r\,K\sin\phi)\,d\phi, \tag{2.42}
$$

which is identical to equation 2.4. Having shown that the self-consistent scheme reduces to the well-known limit, I now focus on interpreting and implementing the scheme.

The scheme relates the quantities r, K, Ω, and α to the set of frequencies $\{\omega_i\}$. To see this, consider the following algorithm:

1. Choose fixed values for Ω and for $r\,K \equiv A$. Note that neither r nor K are known, only their product.

2. Compute $r\,e^{-\imath\,\alpha}$ using the self-consistent expression 2.37.

3. Having obtained a value for r given the fixed value of A, compute $K = A/r$.

The algorithm produces values for r, K, and α for the given values of Ω and $r \cdot K$. I interpret the results of these calculations to mean that if I were to perform a simulation of the Kuramoto model for the given set of oscillators at the computed coupling of K and computed phase offset α, the system would exhibit synchronization with an average value of r at the synchronized frequency Ω. (If I find multiple solutions, then I expect the solution with the largest r to dominate the dynamics.) To predict the outcome of a simulation, I need only tabulate values for r, K, Ω, and α.

Algorithmically speaking, the key difference between the simple self-consistent equation 2.17 and the full self-consistent equation 2.37 is that the latter introduces an extra parameter Ω. In the simple scheme, I take $\Omega = \bar{\omega}$ and I ignore imaginary terms. In the full scheme I vary Ω to find sums in equation 2.37 for which the imaginary component is zero, obtaining a prediction for the original Kuramoto model where $\alpha = 0$. However, with greater freedom comes greater computational expense and tabulating predictions for r, Ω, and α when I only care about the case $\alpha = 0$ wastes computing resources and time. The problem can be recast as a zero-finding search. Highly optimized algorithms exist for zero-finding but these algorithms assume continuity in the function's derivative, and although the piecewise equation 2.37 is continuous its derivative is discontinuous in many places. In order to determine where the discontinuities arise, I next consider the contributions to r due to a single oscillator as a function of Ω.

Equations 2.34–2.36 show how an individual oscillator contributes to the self-consistent calculation for r. I call these contributions $\rho_i(\Omega, r\,K)$. Figure 2.6 shows the real and imaginary parts of $\rho_i(\Omega, r\,K)$ as a function of Ω for a fixed but arbitrary value of $r\,K$, indicated by the solid semicircle. The real component of ρ_i is continuous and has support only over a finite range of Ω, specifically $-r\,K < \omega_i - \Omega < r\,K$. The real component of ρ_i is symmetric about $\Omega = \omega_i$ and is an even function of $\omega_i - \Omega$. The imaginary component of ρ_i is also continuous and symmetric about $\omega_i - \Omega$, but has support over the whole real line

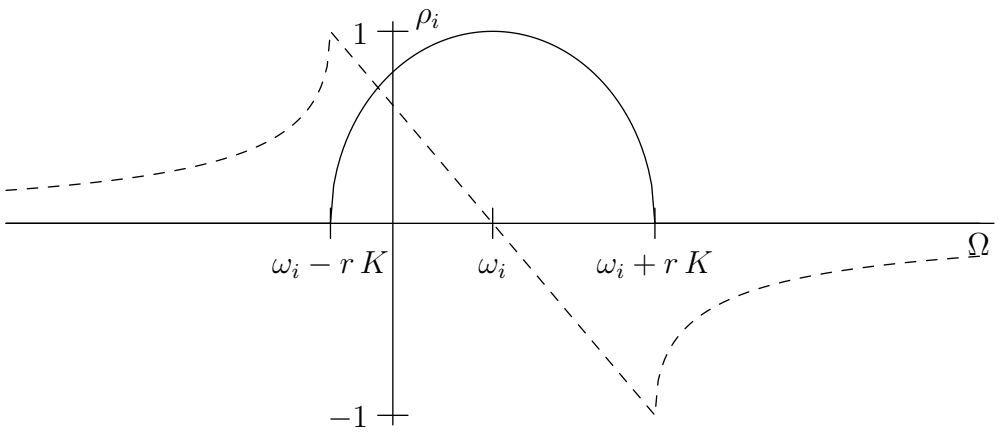

Figure 2.6: Real (solid) and imaginary (dashed) parts of $\rho_i\,(\Omega,\, r\,K)$ for a fixed but arbitrary $r\,K$ and nonzero ω_i.

as indicated by the dashed curve. Furthermore, the imaginary component of ρ_i is an odd function of $\omega_i - \Omega$. For a system composed of a single oscillator, the $\alpha = 0$ solution (zero-crossing) corresponds with $\Omega = \omega_i$ and a magnitude $r = 1$, which agrees with the definitions for Ω and r in the trivial case of a single oscillator. The only zero for this case falls between $\omega - r\,K < \Omega < \omega + r\,K$. (Note that for $\alpha \neq 0$, the synchronized speed Ω is slower or faster than ω_i according to the sign of α, but the magnitude of the complex number $r\,e^{\imath\,\alpha}$ is still 1.)

Figure 2.7 shows a series of real and imaginary order-parameter predictions for three oscillators in which the frequency of the leftmost oscillator is increased from $\omega_1 = -1.9$ to $\omega_1 = -0.7$. The frequencies of the other two oscillators are held fixed at $\omega_2 = 0$ and $\omega_3 = 1.5$, and $r\,K = 1$ is also held fixed. This figure reveals a number of important features. First, $r\,(\Omega,\, r\,K)$ for three oscillators has six kinks and the Ω coordinates for four of them remain fixed as ω_1 changes. The kinks occur at $\Omega \in \{\omega_i \pm r\,K\}$, giving a discrete set of intervals to check for zeroes. Second, all zeroes of the imaginary part of r fall within $(\omega_{min} - r\,K,\, \omega_{max} + r\,K)$; the values of r for Ω outside these regions are either strictly positive for $\Omega < \omega_{min} - r\,K$ or strictly negative for $\omega_{max} + r\,K < \Omega$. Third, the imaginary part of r may possess 0, 1, 2, or 3 zeroes on intervals over which r is continuous.[2]

[2]To prove this, note that the concavity is dominated by the two nearest cusps. These cusps either have

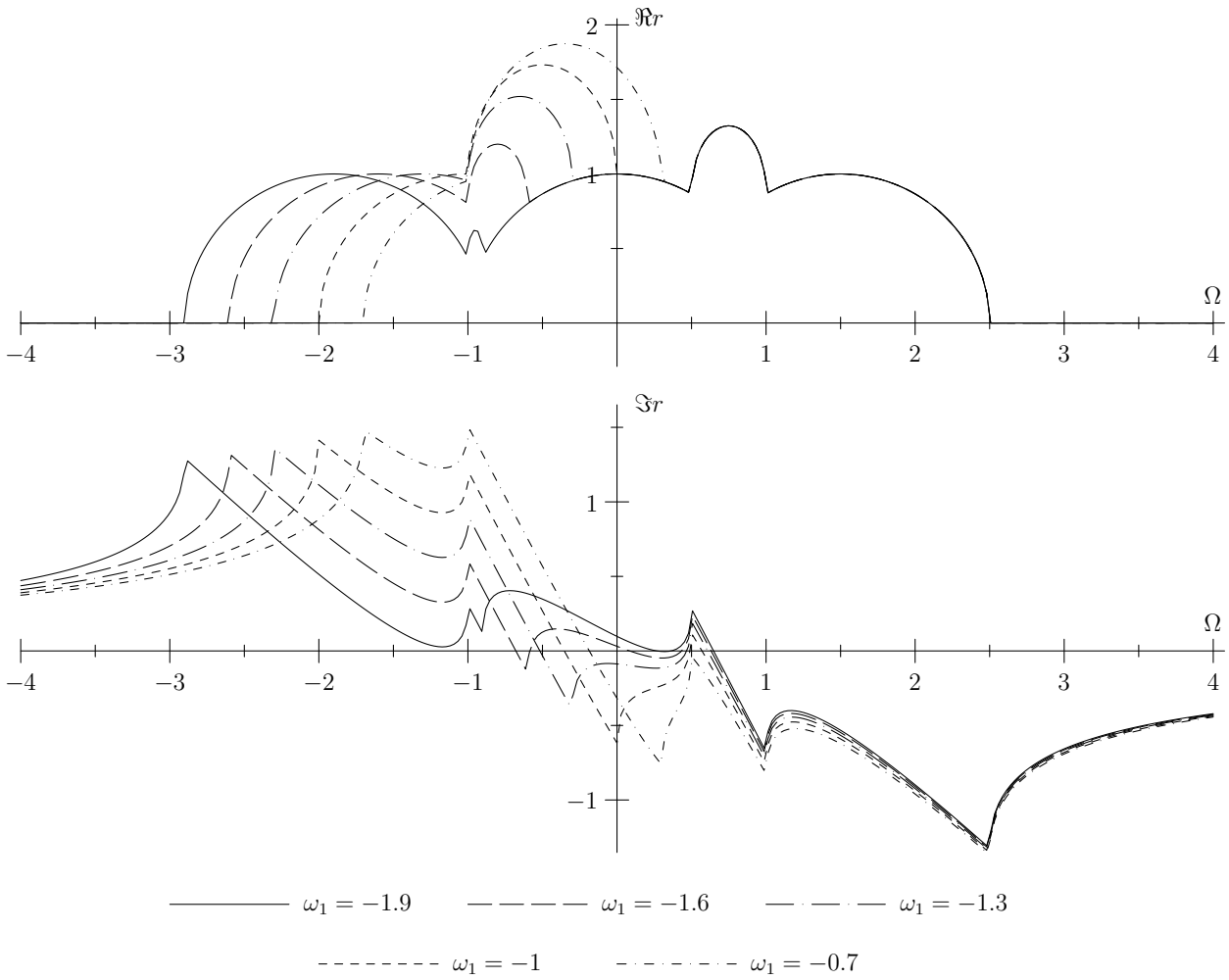

Figure 2.7: Real (top) and imaginary (bottom) parts of $r\,(\Omega,\, r\,K)$ for $r\,K = 1$, ω_1 as marked, $\omega_2 = 0$, and $\omega_3 = 1.5$.

Based on all the observations I just made, one could develop an efficient and complicated algorithm capable of finding all the zeroes of $\Im r$. Due to time constraints, I was unable to implement such an algorithm. Instead, I implemented a much simpler algorithm for finding the zeroes that breaks each known continuous interval into multiple pieces and performs a bounded zero search on each of those intervals. Figure 2.8 shows the simulations initially presented in figure 2.2 plotted against the predictions from the full scheme. To generate this figure, I broke each known continuous interval into 16 distinct subintervals and executed a

the same concavity in which case there is no inflection point, or have opposite concavity in which case there is only one inflection point. A curve with a single inflection point can have no more than three zeroes.

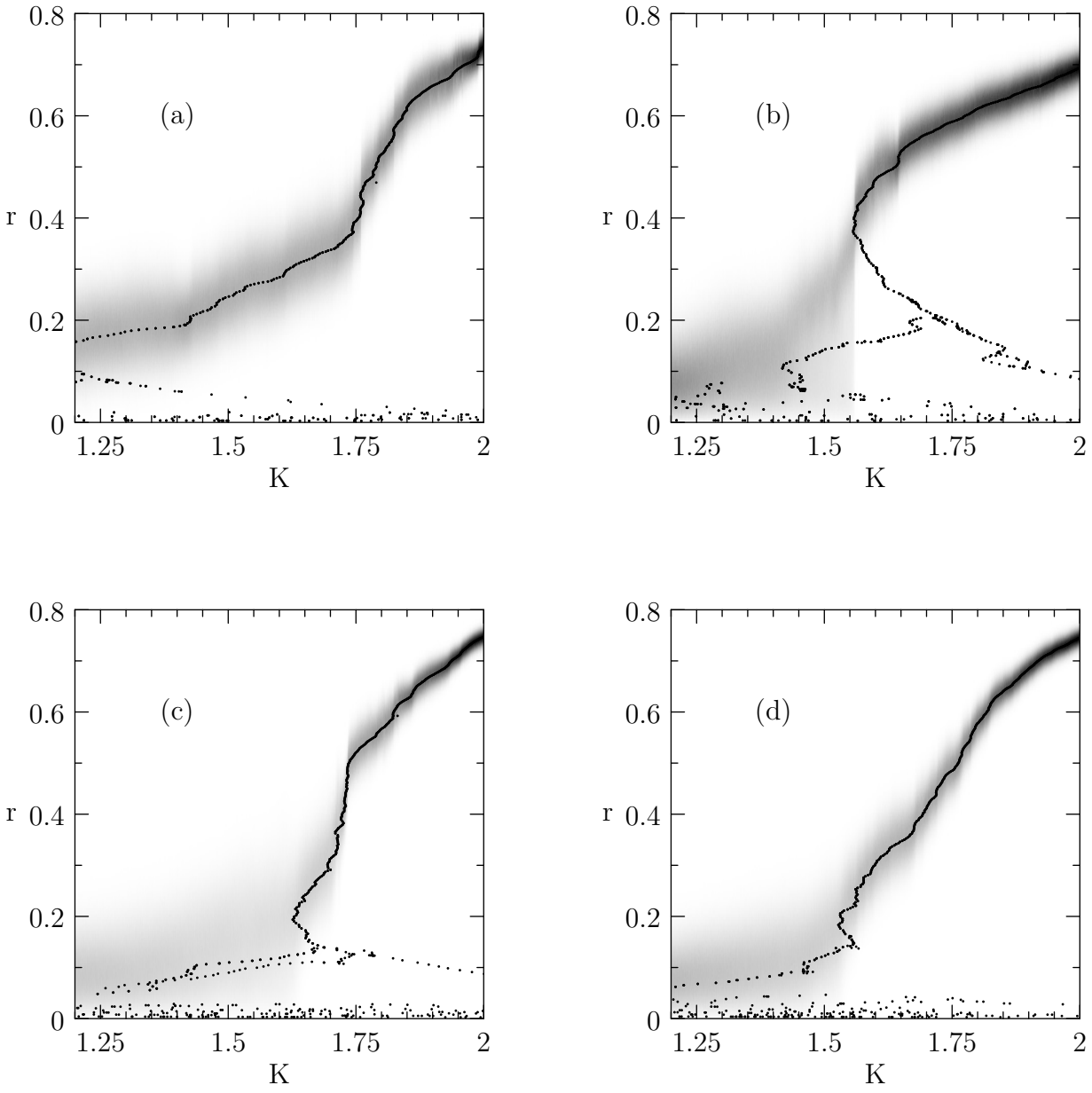

Figure 2.8: Predictions for the full scheme compared to numerical simulations, as shown in figure 2.2. Compared to figure 2.4, which shows the predictions assuming $\Omega = \bar{\omega}$, these predictions perform much better for the unsymmetric populations depicted in figures (c) and (d).

bounded zero-finding algorithm on each. The resulting predictions for populations (a) and (b) agree with those of figure 2.4, but the predictions for populations (c) and (d) perform much better than those shown in figure 2.4. In particular, the failures for the non-symmetric populations are easy to identify from the predictions alone and correspond with substantial changes in the simulations' behavior.

As shown, the predictions cannot be easily compared with the numerics. Some of the predictions shown in figure 2.8 appear to closely match the simulations, but they are peppered with extraneous results. I stated earlier that if I find multiple solutions to self-consistent scheme, I expect the prediction with the largest r to dominate and the numerics clearly support that interpretation. To clean the data, I bin the (K, r) predictions by their r-values into 300 uniformly spaced r-bins from 0 to 1 and for each bin select the pair with the minimum K value (the left-most pair). The resulting data resemble the simple self-consistent curves plotted in figure 2.4 except they better track the numerics for populations (c) and (d). In particular, for many values of K they give multiple predictions for r. The multi-valued character of these data is a feature: it allows me to construct the $r\,(K)$ predictions as a collection of piecewise-continuous predictions with discontinuous jumps. Such a construction, for population (d), is shown in figure 2.9. At the end of this rather involved cleaning process, I have a collection r_{sc} of piecewise monotonic predictions for r vs K that can be compared to the numerical simulations. I also explicitly know the values of K at which r_{sc} exhibits discontinuities.

Figure 2.10 demonstrates how the full self-consistent scheme's predictions fare against the average order parameter from the direct numerical simulations. I computed the values for the averaged order parameter from the results of the direct numerical simulations using a weighted average:

$$\bar{r}\,(K) = \frac{\sum_i r_i n_i}{\sum_i n_i}. \tag{2.43}$$

Above each of these difference curves I plot the discontinuities in the self-consistent scheme, also as a function of K. The following properties immediately emerge:

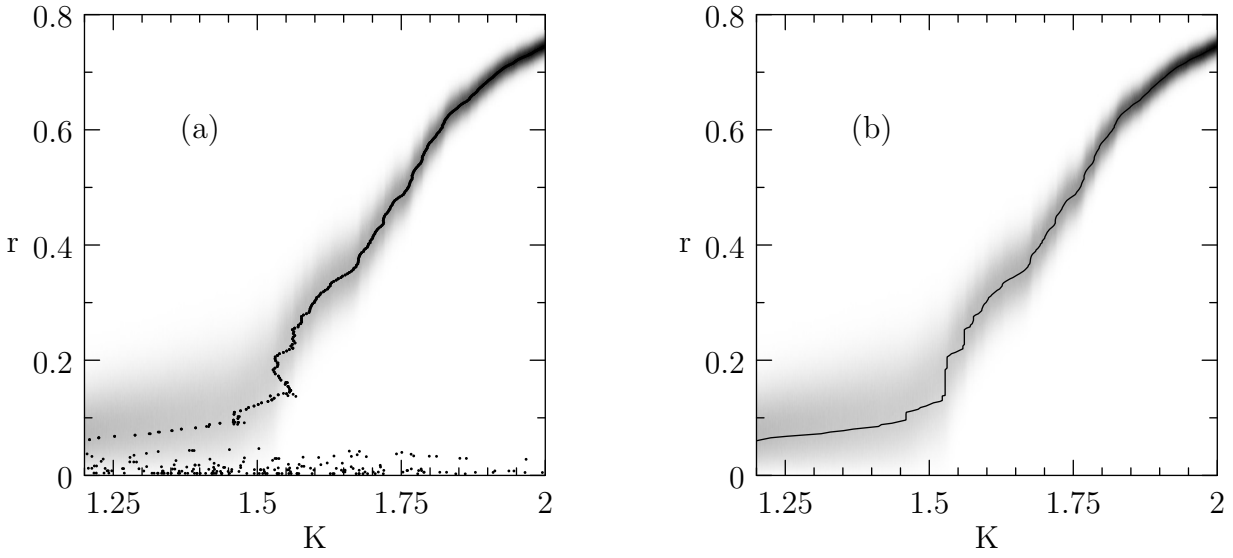

Figure 2.9: Results of cleaning the data from the full self-consistent scheme, as demonstrated for population (d). The original predictions are shown in (a) (reproduced from figure 2.8d); the cleaned results are in (b).

1. The scheme performs very well for $K \gtrsim 1.8$, but is also consistently below the numerical average.

2. Many features in the difference plot $r_{sc} - \bar{r}$ are quite narrow. Others, especially where r_{sc} differs from $\bar{r}$, are rather broad.

3. Though r_{sc} is generally less than $\bar{r}$, the largest (and sometimes the second-largest) discontinuity usually accompanies a positive spike in $r_{sc} - \bar{r}$.

4. Except for population (a), the largest discontinuity corresponds with a significant change in quantitative accuracy.

The fluctuations ignored in calculating r_{sc} apparently lead to consistently larger values in the real order parameter, even for relatively large values of K and r. I did not expect this. It may be possible to extend the scheme by using an effective coupling $f(\psi - \theta_i)$, where f is similar but not identical to a sine function. However, such a form would likely lead to intractable calculations for the unentrained oscillators, and a full treatment of the fluctuations would probably be a better course of research.

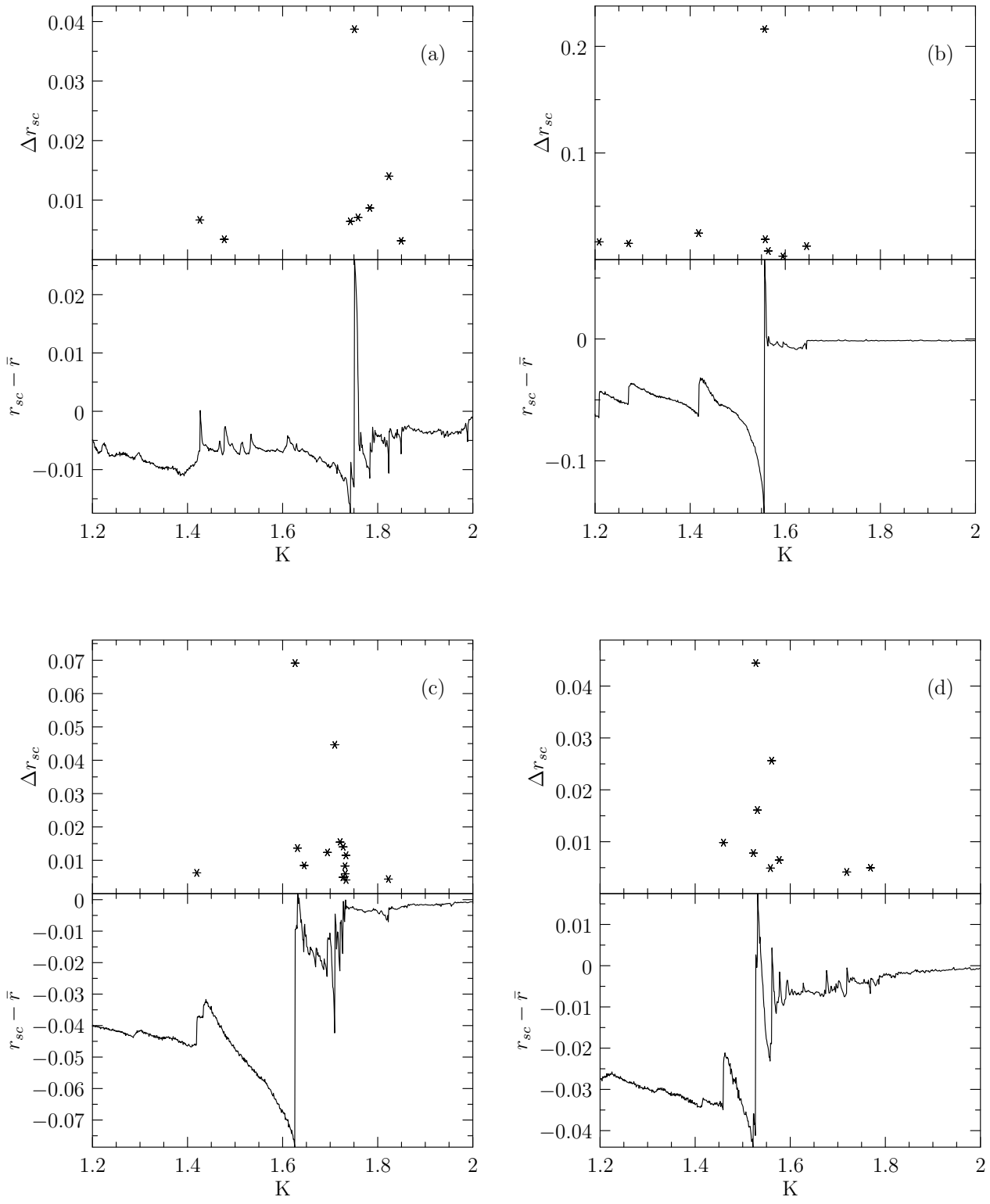

Figure 2.10: Discontinuities for the full self-consistent scheme and comparisons of the average order parameter $\bar{r}$ from the direct numerical simulations to the prediction r_{sc} of the full self-consistent calculation.

Sharp features in $r_{sc} - \bar{r}$ versus K have a very simple interpretation: both r_{sc} and $\bar{r}$ show swift changes for close but non-identical values of K. Discontinuities and steep slopes in r_{sc} for values of K above the largest discontinuity accurately predict swift changes in the numerics. Also, the unusual positive behavior near the largest discontinuities arises because the scheme's largest jumps occur just before the end of the swiftest behavior in the numerics. Discontinuities are accurate predictors of swift changes in the real system.

Broader features in Figure 2.10 have an equally clear interpretation: r_{sc} and $\bar{r}$ have substantially different slopes over an extended range in K. For example, for K between 1.45 and 1.55 in population (b), $\bar{r}$ grows roughly from 0.2 to 0.3, getting faster as it approaches the sudden transition at $K = 1.55$. In contrast, the scheme predicts a consistent and slower rate in increase followed by a sudden huge jump at $K = 1.55$. The difference in slopes leads to the broad drop in $r_{sc} - \bar{r}$ as K runs from 1.4 to 1.55.

In general, the scheme captures nontrivial, nongeneric features when r is not small. It also gives clear signatures for where where it will fail, and those signatures correspond to interesting behavior in the direct numerical simulations.

2.5 Conclusion

In this Chapter I have demonstrated I can make accurate, population-specific predictions for the Kuramoto model by assuming the mean field has a constant magnitude r and steady rate of rotation Ω. All the oscillators in the population contribute to the self-consistent expression and non-symmetric distributions show predictions for r that require values of Ω that do not correspond to the population's mean velocity $\bar{\omega}$. Taking those contributions into account leads to predictions that are accurate over a wide range of K, and which have clear indications when they are close to failing.

One of the most important outstanding questions from this work is whether the smaller discontinuities predicted by the self-consistent scheme correspond to real discontinuities in

numerical simulations. I have preliminary numerical evidence that larger populations ($N = 4096$) exhibit finite (bistable) switching behavior near scheme-predicted jumps. It appears that for my population size of $N = 512$, finite-size effects have washed out discontinuous behavior. Whether or not the numerics exhibit jumps, I am confident that the discontinuities in the scheme correlate with swift behavior in the numerics, and I next study the scaling properties of these discontinuities in their own right.

Chapter 3

Critical Behavior in the Simple Scheme

As noted in the Introduction, the Kuramoto model exhibits a continuous phase transition in the limit $N \to \infty$. The explanation of critical behavior near phase transitions was one of the great theoretical accomplishments in twentieth century condensed matter physics and many texts and reviews explain the renormalization approach to the problem [16, 17]. The Kuramoto model also exhibits critical phenomena near the critical coupling strength K_c. In this Chapter, I describe my work studying avalanching—one kind of critical behavior—in the simple scheme developed for the Kuramoto model that I presented in the last Chapter.

From the standpoint of statistical physics, avalanching is the notion that a continuous phase transition in a finite-sized system actually occurs as a collection of discrete jumps. Microscopically, one imagines a system of discrete units (atoms, magnetic domains, oscillators) whose behavior can resemble one of two phases; when one of the units changes behavior, the global measurement of the system shows a discontinuous jump. Furthermore, one unit's change may cause other units to change their behavior as well, leading to a cascade of changes. Such cascades are called avalanches and avalanching reveals itself as a critical phenomenon when the distribution of jump sizes exhibits a power law with properties that depend on the system's proximity to the critical point.

Though he did not search for avalanches, Daido developed the majority of the work on finite-size effects in the Kuramoto model in the second half of the 1980s [18, 19, 20, 21, 22]. Kuramoto and Nishikawa also published a few related papers, but they focused on determining the globally stable state in the large-N limit [23]. In a series of papers Daido showed first numerically and then analytically that the model exhibits divergent behavior

Exponent	$K < K_c$	$K > K_c$	Definition
γ'	$1/2$	$1/8$	$\sqrt{N}\left\langle \lvert r-\bar{r}\rvert^2 \right\rangle^{1/2} \propto \lvert K-K_c\rvert^{-\gamma'}$
p	1	$1/4$	$\tau_c \propto \lvert K-K_c\rvert^{-p}$
s	$1/2$	2	$\lvert K_c(f)-K_c\rvert \propto N^{-s}$
$\nu = 1/s$	2	$1/2$	$N_c \propto \lvert K-K_c\rvert^{-\nu}$, $N\Delta_c \propto N^{-1}\lvert K-K_c\rvert^{-\nu}$

Table 3.1: Daido's Critical Exponents

when K is near the critical coupling K_c, as determined by the large-N limit. In his final paper on the matter [22], Daido presented his fully developed theory for the exponents along with a reproduction of the numerical results. Daido's exponents exhibit the remarkable feature that the values for $K < K_c$ differ from those for $K > K_c$. Mean-field models typically have the same scaling exponents below and above the critical point, making the Kuramoto model unique among mean-field models. Unfortunately, Daido's analysis depends critically upon a complicated equation that he states without derivation and his writing is impenetrable. Further work in the Kuramoto model focused on determining the stability of the globally attracting state, spurred by the work of Strogatz and Mirollo, who reformulated the $N \to \infty$ problem and published rigorous predictions for the stability of the synchronized state [3]. Strogatz and Mirollo's work kicked off a new direction of interest for the Kuramoto model, but future examinations of finite-size effects focused on modified models, such as considering the Kuramoto model with additive noise [24].

Daido's main results are summarized in table 3.1. Daido first became interested in the critical behavior of the Kuramoto model when he found substantial fluctuations in the order parameter near the critical point. The RMS fluctuations scale with $|K - K_c|$, the system's vicinity to the critical point, according to γ'. Individual deviations in r can be long-lived and the second exponent p gives the scaling of the durations of those deviations, τ. Compared with larger systems, smaller systems show critical behavior over a larger range in K, and the range of K over which the system displays appreciable finite-size fluctuations, $K_c(f) - K_c$, scales with the system size according to the exponent s. The related exponent ν describes the scaling of the critical population size N_c that shows fluctuations at a given distance from

the critical coupling K.

On the one hand, the assumption in the scheme that r is constant explicitly contradicts Daido's work. However, the scheme also exhibits finite discontinuities, and Richard and I—in conversation with Karin Dahmen—hypothesized that the discontinuities may capture the critical behavior in the Kuramoto model, in spite of the non-physical assumption of constant r. After all, avalanching of this sort has been observed in magnets and the scaling theory for the Ising model correctly predicts the critical phenomena in magnets in spite of its many simplifications [25]. Furthermore, the Kuramoto model resembles the Heisenberg model for magnets, which exhibits scaling behavior that has been mapped to the Ising model. So, I set out to study the critical behavior of the discontinuities in the Kuramoto model.

3.1 Method for Finding Avalanches in the Scheme

Both the simple scheme (Section 2.2) and the full scheme (Section 2.4) demonstrate backtracks, portions of the r vs K curves in which r increases as K *decreases*, as shown in figure 2.8. Population (b) shows a large backtrack, the top of which is near $r = 0.4$, $K = 1.55$, and a small backtrack near $r = 0.5$, $K = 1.65$. Population (c) shows a small backtrack for r between 0.15 and 0.2, at about $K = 1.65$. The predicted curves contain many other indiscernible backtracks, as highlighted in the example in figure 3.1. If I assume that the system always follows the largest value of r for a given value of K, as confirmed in the previous Chapter, then the backtracks imply discontinuous jumps in r. This assumption is not true for large discontinuities in small populations—a feature of the scheme which tells me where to look for interesting changes in the system's behavior—but may hold reasonably well for smaller discontinuities exhibited by larger populations. In what follows, I analyze the distribution of these jumps in the hope that their statistics shed light on avalanching behavior in the Kuramoto model for larger populations.

The numerical scheme offers a major advantage over direct numerical simulations: speed.

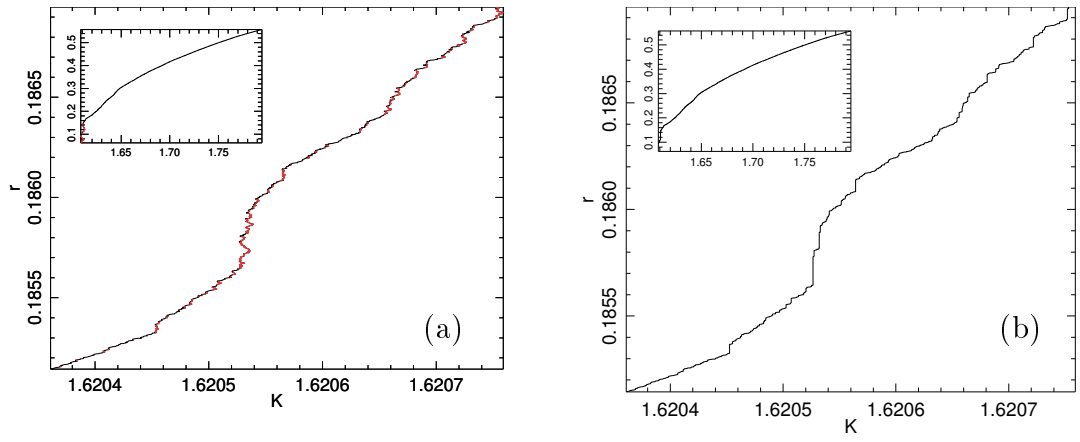

Figure 3.1: The method for computing discontinuities in r simply replaces backtracking behavior in figure (a) with discontinuous jumps, depicted as vertical lines in figure (b). The insets show a much larger range in K, for context.

The study of avalanching requires a large quantity of data yet Daido's exponents show that the lifetime of fluctuations in the order parameter diverges near the critical coupling. Measuring tiny changes in the order parameter would require exceedingly long simulations. In contrast, the scheme computes its predictions very quickly (relative to direct numerical simulations) making it much better suited for gathering the necessary quantity of data to achieve a meaningful scaling collapse.

In the following analysis, I take the scaling forms from the study of the Ising model by Perković, Dahmen, and Sethna [25]. Perković et al.'s equation 49 describes the avalanche size distribution as a function of avalanche size S, system disorder R, and external field H. I only consider the undriven Kuramoto model, so my system does not have an analog to the external field. I also seek scaling in the coupling K rather than the disorder R. Modifying the scaling function appropriately, I expect the distribution of avalanches to scale as

$$D\left(\Delta r,\, K\right) \propto \Delta r^{-\tau} \mathcal{D}_{\pm}\left(\Delta r \left|K - K_c\right|^{\alpha}\right). \tag{3.1}$$

$\mathcal{D}$ is an unknown scaling function; it and the scaling exponents α and τ should emerge in the process of performing the scaling collapse. (In Perković et al., the scaling exponent in the argument of the scaling function is σ and it is placed on Δr so that in their notation

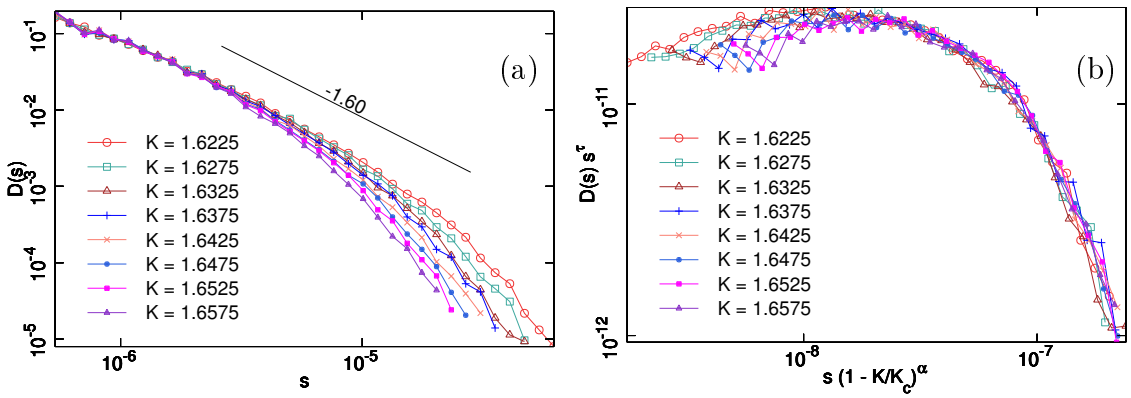

Figure 3.2: Scaling collapse of avalanche distributions in the simple scheme for $N = 10^6$. In these figures s represents the step size Δr. For figure b, the values of the exponents are $\alpha = 1.4$, $\tau = 1.6$. The line with slope -1.6 shown in figure (a) is a guide to the eye.

$\alpha = 1/\sigma$.)

Note that the number of oscillators that become synchronized in a discontinuity of size Δr is roughly $N \cdot \Delta r$, meaning that the label "avalanche" only makes physical sense when the jumps exceed N^{-1}. (A claim that 0.1 oscillators suddenly synchronize seems dubious at best.) The scheme can predict smaller discontinuities, but labeling them as avalanches is not appropriate.

3.2 Avalanching in the self-consistent scheme

Figure 3.2 shows my first and most successful attempt at finding critical avalanching in the Kuramoto model. It displays the combined distribution of avalanches for many populations of $N = 10^6$ oscillators. The uncollapsed data in figure (a) follows a power law with an exponential cutoff for large Δr. However, figure 3.2(a) is peculiar in a number of ways. The largest shown avalanche size, $\Delta r \approx 5{\cdot}10^{-5}$, corresponds to about 50 oscillators synchronizing, which is a small number compared to the population size. Also, the range of K bins runs from 1.62 to 1.66, which avoids data closest to the critical coupling $K_c \approx 1.6$. Subfigure (b) shows an excellent collapse of the data, but unfortunately many other values of the parameters α, τ, and K_c gave equally or nearly equally good results. Although I presented the results of

figure 3.2 at the 2010 March Meeting, I have forgotten why I chose such restricted ranges of Δr and K and I subsequently lost the original data and some of the code that produced them due to a hard-drive failure. Nonetheless, the scaling behavior in figure 3.2 covers over a decade of physically meaningful avalanches and the collapse itself is excellent.

Spurred by my success for $N = 10^6$, I next sought to perform similar collapses for smaller populations. In addition to providing additional estimates to the parameters α and τ, combined collapses for multiple population sizes provide a means for computing relations between α and τ, leading to restrictions in the otherwise wide range of parameters that result in successful collapses.

My attempts at scaling collapses for smaller populations ($N = 10^3$ and $N = 10^4$) are shown in figure 3.3. Subfigures (a) and (c) show the distribution of avalanches on a log-log plot and they clearly show power-law behavior for all but the largest avalanche sizes. However, they exhibit a bump on the end of the distribution representing the largest avalanches, and the curves cross at the tips. I will examine this unusual and worrisome characteristic after explaining the scaling collapses. Subfigures (b) and (d) show the scaling collapses which, unlike the collapse in figure 3.2, I plot on linear x- and y-axes. The collapses appear to perform fairly well, but just like the data for $N = 10^6$ they do not have discriminating power. In an attempt to relate the exponents of these collapses to the one shown for the larger population, I performed a collapse at $\tau = 1.6$, as shown in figure 3.4. Although I had to consider a narrower range in K for $N = 10^3$, the collapses perform about as well for $\tau = 1.6$ as their counterparts shown in figure 3.3.

The cross-over behavior of the distributions plotted in figures 3.3 (a) and (c) lead to one glaring problem with the scaling collapses in the associated subfigures (b) and (d): α *is negative.* If the underlying scaling function is bell-shaped, then a negative value for α makes no sense. Such a value implies very few large avalanches occur in the vicinity of the critical coupling, and that the largest avalanches only occur further from the transition. Not only does a negative value for α contradict the scaling collapse for $N = 10^6$ oscillators, but it also

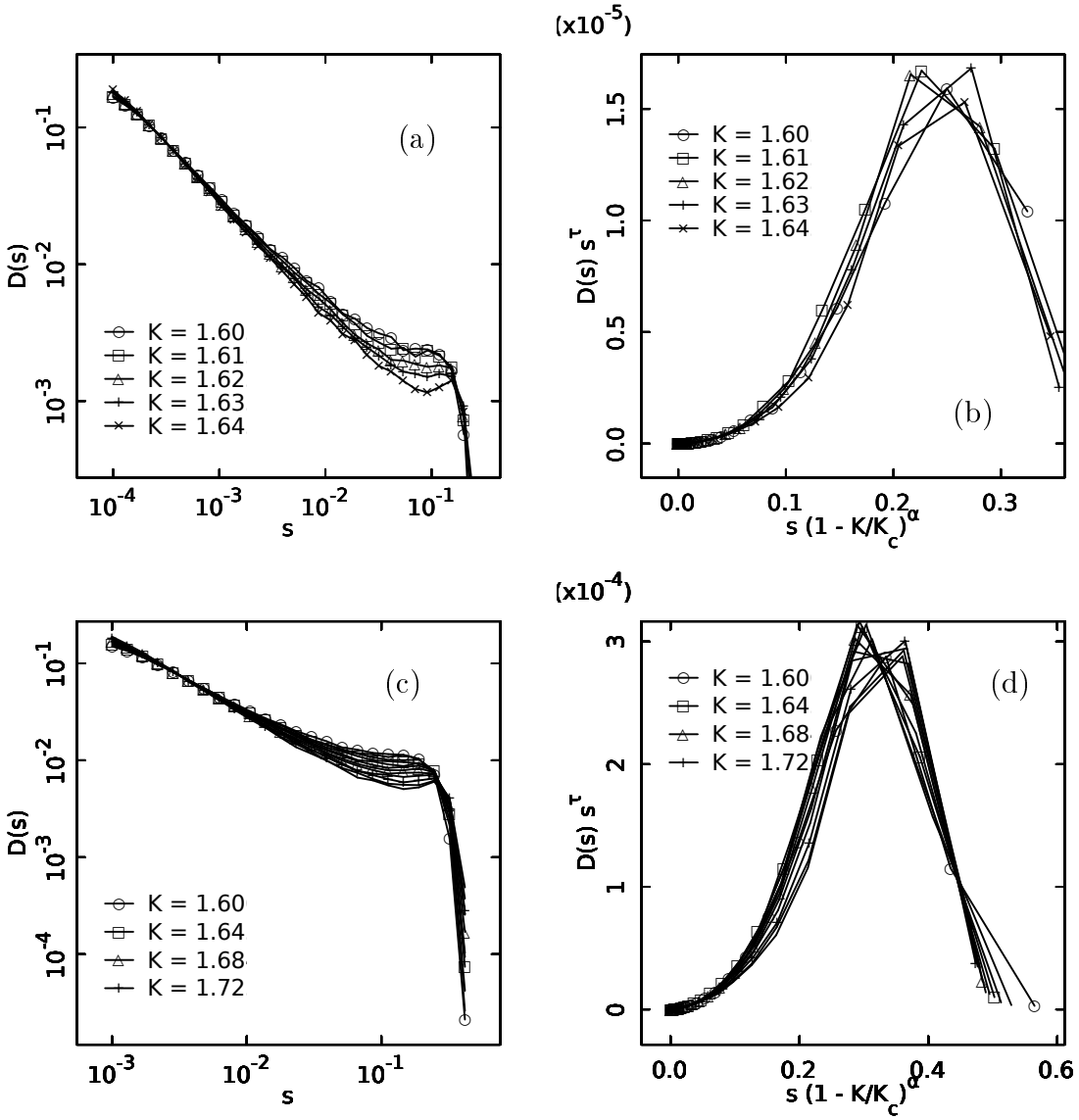

Figure 3.3: Distributions of avalanche sizes (a, c) and scaling collapses (b, d) in the simple scheme for $N = 10^4$ (a, b) and $N = 10^3$ (c, d). As in figure 3.2, s represents the step size Δr. In figure (b), the values of the exponents are $\alpha = -0.09$, $\tau = 2.5$ and in figure (d), the values of the exponents are $\alpha = -0.06$, $\tau = 2.3$. Note that the figures (b) and (d) are linear plots, and the sign of α is indeed negative for both of them. Also note that for figures (c) and (d), the range in K values is much wider than for the other plots.

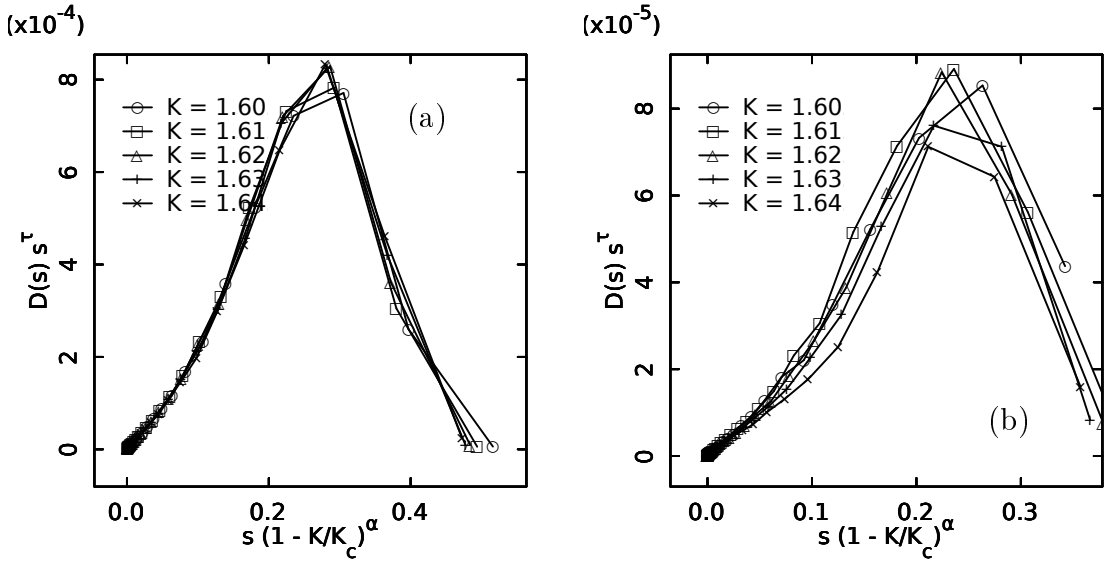

Figure 3.4: For comparison to the case $N = 10^6$, these show scaling collapses for $N = 10^3$ (a) and $N = 10^4$ (b) for K between 1.6 and 1.65 and for $\tau = 1.6$. In (a), $\alpha = 0$ whereas in (b) $\alpha = -0.1$.

disagrees with Daido's work, which indicated divergent behavior near the critical coupling K_c. Even if I cut out the most offensive data and restrict the scaling collapse to smaller values of Δr, which appears to be what I did for the million-oscillator collapse, the upward concavity due to the bump at the end of the distributions causes all attempts of a collapse to diverge.

3.3 Conclusion

In this Chapter, I have demonstrated that the distribution of discontinuities in the simple self-consistent scheme does not scale in the standard way.

In retrospect, I am not surprised. In the last Chapter I demonstrated that the scheme most accurately predicts the direct numerical simulations for couplings above the largest scheme-predicted discontinuity. Above the largest avalanche, where agreement is good, the avalanches correspond with swift changes in the numerics and the magnitudes of the avalanches roughly agree with the magnitudes of the changes in the numerics. Although the

largest avalanche accurately predicts swift changes in the numerics it typically overestimates the magnitude of the change, and below the largest avalanche the scheme's predictions of discontinuities have no relation with the behavior of the numerics. Daido showed that the Kuramoto model exhibits critical behavior for K near K_c, and by extension the accurate predictions should also exhibit critical behavior. However, the inclusion of the inaccurate predictions seems to have destroyed the most sensitive and important end of the avalanche distribution corresponding to the largest jumps.

Although the self-consistent scheme gives remarkably accurate predictions, unfortunately it is no replacement for direct numerical simulations for studying the critical behavior of the finite Kuramoto model.

Part II

Resonant Coupling

Introduction to the Second Part

I spent the first part of this dissertation closely examining the Kuramoto model. In this the second part of the dissertation, I examine an experimental system that is a close relative of the Kuramoto model. In Chapter 4 I discuss the experimental setup, the methods used to take measurements, and the key results of the measurements. In Chapter 5 I discuss a simple mechanical model that reproduces the key collective behavior observed in the laboratory and I compare it to the Kuramoto model. The original Kuramoto model does not capture the key behavior of the experimental system, but a modified model with only two new features—frequency-dependent coupling and a frequency-dependent phase delay—explains the behavior very well.

Chapter 4

Synchronization with Resonant Coupling

Experimental studies of synchronization are numerous. Biological examples abound [26, 27, 28], but synchronization occurs in many other systems, including coupled metronomes [29], laser arrays [30], chemical oscillators [31, 32, 33], and arrays of convective cells [34]. Lasers [30, 35], thermo-acoustic engines [36, 37, 38], Josephson junctions [39, 40, 41, 42], metronomes [29], and pendulum clocks [43] have also been studied. Perhaps the most notorious example of collective synchronization occurred among pedestrians crossing the Millennium Bridge in London when it first opened [1]. These systems are all examples of populations of similar but not identical oscillators that exhibit the same basic patterns of behavior, that (1) they synchronize spontaneously, without the need for any external driving, and (2) as the oscillators' coupling increases, their synchronization strengthens. The two systems most similar to the work I discuss in this Chapter are the Pantaleone's metronomes and the study of the Millennium Bridge. The key difference between my work and other work in synchronization is that I consider the resonant character of the coupling to be a feature of the system, not something to be suppressed.

In this Chapter I present an experimental system that exhibits synchronization: small mechanical vibrators coupled through a resonant plate. The coupling between the oscillators depends on frequency and exhibits a simple resonance structure. How does frequency dependent coupling effect the dynamics of coupled oscillators? Unlike the simple Kuramoto model, I find history-dependent behavior due to characteristic interactions with the resonances of the plate. The frequencies of individual motors tend to level-off just below plate resonances and motors tend to avoid frequencies just above resonances. Groups of motors show similar

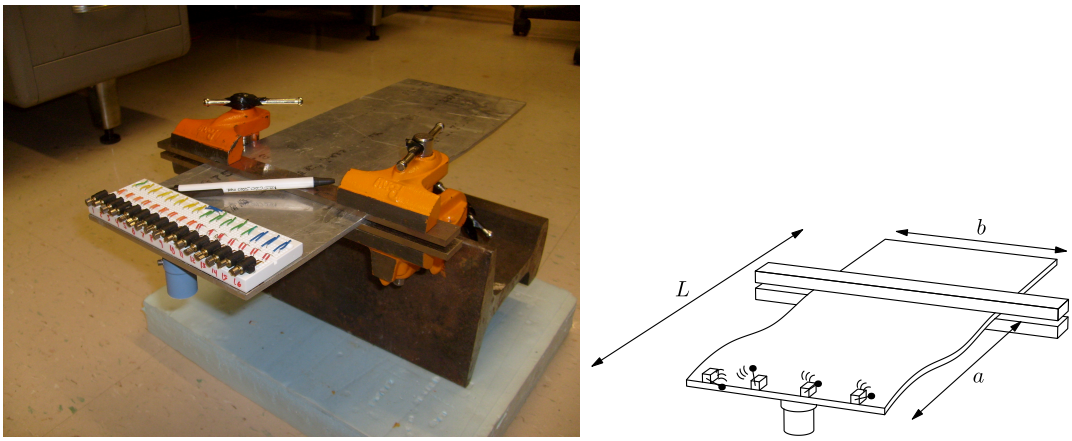

Figure 4.1: A photo and diagram of the experimental setup, as described in the first section.

features but have wider hysteresis loops because the leveling-off of the frequencies below a resonance extends to higher driving voltages than individual motors. The non-transient behavior of the motors operating at a fixed voltage seem to show that the average motor velocity is roughly constant.

4.1 Experimental Setup

My experiment involves 16 small motors with eccentrically massed rotors. The motors (All Electronics Corporation, catalog number DCM-204[1]) are small dc motors, the sort used as vibrators in mobile phones. Each motor has a mass of $3\,g$ and is $2\,cm$ long, $1\,cm$ high, and $1\,cm$ wide. Each motor's rotor has a center of mass that is offset from the axis of rotation, with a first moment of $0.74\,g\text{-}mm$. Vibrations arise from the rotation of this off-center mass. (For a clearer picture of how the motors interact with and through the plate, see Chapter 5.)

I glue the motors to a breadboard which is itself glued to a mechanically compliant and resonant aluminum plate. The motors interact indirectly through the plate, which is held by clamps as shown in figure 4.1. The plate is $L = 115\,cm$ long, $b = 15\,cm$ wide, and

[1]This item is no longer available in the catalog, but similar motors can be found in their catalog searching for "motor vibrator."

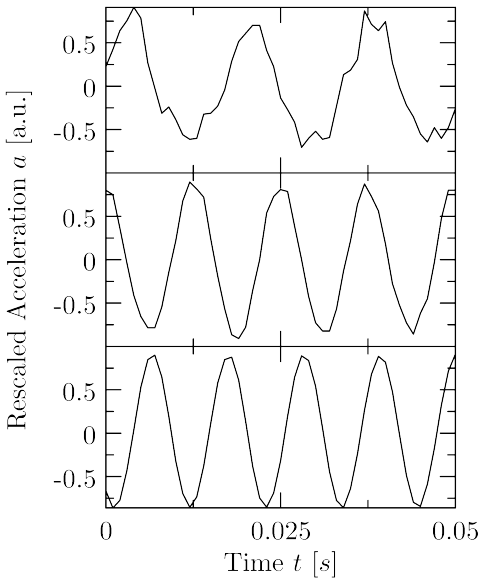

Figure 4.2: Typical time series of a single motor on the plate for different voltages. From top to bottom, the data correspond to driving voltages of $0.65\,V$, $0.84\,V$, and $1.05\,V$.

$5\,mm$ thick. I adjust the linear response of the system by adjusting the location where the clamps hold the plate, parametrized by the length a. Although I considered various clamp positions, I will only discuss results based on a length of $a = 12.5\,cm$, for which the system has resonances at $68\,Hz$ and $100\,Hz$.

I measure the plate's vertical acceleration $a\,(t)$ using an accelerometer attached to the plate, a PCB 353B33. In the diagram shown in figure 4.1, the accelerometer is depicted by the canister underneath the motors. Figure 4.2 shows a few typical time series of acceleration data due to a single motor. The sampling rate for these and all other data is $r = 1000$ samples per second. The plate is a linear medium, so I attribute any observed vibrations either to the motors or to background sources, such as building vibrations. In order to reduce spurious frequencies from the environment, I place the entire setup on a foam pad. Although some background noise still perturbs the system, these vibrations do not dominate the signal reported by the accelerometer and have frequencies much lower than the motors' primary frequencies.

Apart from quantitatively measuring the system, I also listen to and watch the system.

The plate creates a great deal of noise, especially when many motors operate near a resonance, making certain transitions immediately apparent just by listening. I observe the system visually using a stroboscope, which allows me to identify the motors' primary frequencies and observe variations of those frequencies. I can also examine the mode-shapes of the plate using the stroboscope. I find that both resonances, near $f = 68\,Hz$ and $100\,Hz$, do not have any nodes along the array of motors and that the displacements of all the motors have about equal magnitude. As such, the couplings between the motors and the plate have no appreciable position dependence. Since the motors interact with each other through the plate, this means each motor interacts equally with all the others.

All of the motors operate from a common power supply, which has important implications for the experimental design. First, small variations in each of the motors mean that, despite operating at the same voltage, all the motors have different natural frequencies. I have not characterized the distribution of motor speeds in any rigorous way but stroboscopic observations indicate that the frequency distribution is approximately unimodal. Second, a common power supply couples the motors electrically, which may lead to synchronization independently of the mechanical coupling. I find that the motors do not show synchronization when run on a massive support (which provides minimal mechanical coupling) so I attribute the synchronization results in the later sections to mechanical interactions moderated by the plate. Third, because I cannot independently change the power delivered to an individual motor, I cannot precisely control the distribution of natural frequencies for a given experimental run. However, the distribution of the natural frequencies of each of the motors at different voltages remains roughly unimodal.

4.2 Behavior of a Single Motor

In order to discuss how multiple motors interact I must first characterize how a single motor behaves, and in order to characterize single-motor behavior, I must develop an automated

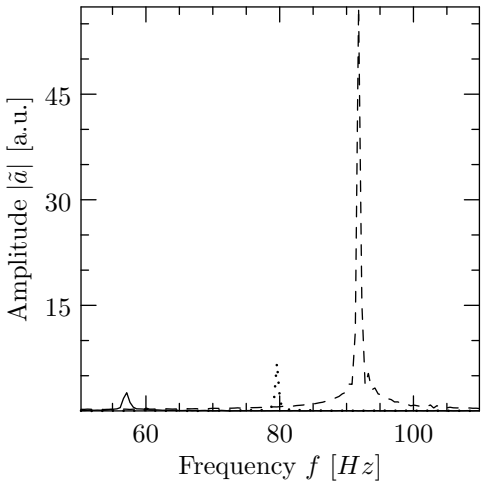

Figure 4.3: Typical Fourier transforms of a single motor on the plate for different voltages. The driving voltages are $0.65\,V$ (—), $0.84\,V$ ($\cdots$), and $1.05\,V$ (- -).

method for reliably extracting a single motor's frequency of oscillation from a time series. After developing such a method, I discuss how an individual motor's primary frequency depends on the driving voltage and then I measure how the plate's response magnitude depends on the motor's primary frequency. I conclude by explaining how I modify raw power spectra to obtain a representation for motor density as a function of frequency.

Figures 4.2 and 4.3 demonstrate typical single motor data at voltages $V = 0.65\,V$, $0.84\,V$, and $1.05\,V$. Both figures show stable periodic behavior. From two-second long data sets $a\,(t)$, sampled at 1000 samples per second, I construct spectra $\tilde{a}\,(f)$, shown in figure 4.3 using a short-time Fourier Transform:

$$\tilde{a}\,(f) = \int_T a\,(t)\, e^{\imath\, 2\,\pi\, f} dt, \tag{4.1}$$

as implemented with an FFT. The Fourier transform gives data for frequencies spanning from $0\,Hz$ to $1000\,Hz$, but the motors' primary frequencies fall into a much narrower range. Using spectroscopic observations and time-frequency plots, I manually determine the minimum and maximum operating frequencies of the motor for a given collection of samples and I only examine Fourier Transform data within those extrema. Usually the motors operate between $f = 40\,Hz$ and $100\,Hz$, but my fastest motors at their highest frequencies could achieve

frequencies up to $170\,Hz$.

To determine a precise measurement of a motor's primary frequency $\hat{f}$, I begin with the frequency corresponding to the maximum amplitude, $\max|\tilde{a}|$, within the pre-determined extrema. Because the short-time Fourier transform uses discrete data, the frequency of the maximum amplitude will come from the set of consecutive frequencies $\{f_1, f_2, \ldots, f_N\}$ with separation $f_{i+1} - f_i = \Delta f = 1/N/\Delta t$. N is the number of samples (2000 for these data) and Δt is the time between samples, $10^{-3}s$, so $\Delta f = 0.5\,Hz$. A plate resonance could be responding to a harmonic of the motor's primary frequency, so if the amplitude corresponding to half that frequency shows a strong peak (a peak with magnitude at least $1/10$ the magnitude of the identified peak), I select that as my rough estimate for the motor's primary frequency. Denote the index of that frequency by i_{peak}.

Having obtained a rough estimate for the motor's primary frequency (accurate to within $0.5\,Hz$), I obtain a precise measurement using a simple weighted average of the frequencies in the vicinity of i_{peak}. Although I considered fitting the data in the vicinity of the peak to a Lorentzian, noise in the tails of the fit often caused the fits to mischaracterize the width of the fit. Instead, I compute a number of estimates for primary frequency $\hat{f}$ by performing the following weighted averages:

$$\hat{f}_n = \frac{\sum_i |\tilde{a}_i|^2 f_i}{\sum_i |\tilde{a}_i|^2} \tag{4.2}$$

where the sums run from $i_{peak} - n$ to $i_{peak} + n$. As n increases, the sum includes more data from the tails of the peak. Because the average is weighted using the squared amplitude, $\hat{f}_n$ reaches stable values once n takes the sum beyond the extent of the peak. I find that including all data points within $5\,Hz$ of the peak is more than enough to give good estimates of the motor's primary frequency, and all such frequency values agree with measurements taken with the stroboscope. For my data, which involves records with durations of $2\,s$, this amounts to assigning $\hat{f} = \hat{f}_{10}$. Using this technique, the primary frequencies verses the driving voltage are plotted for the motor on a plate or on a massive block in figures 4.4(a) and 4.4(b), respectively.

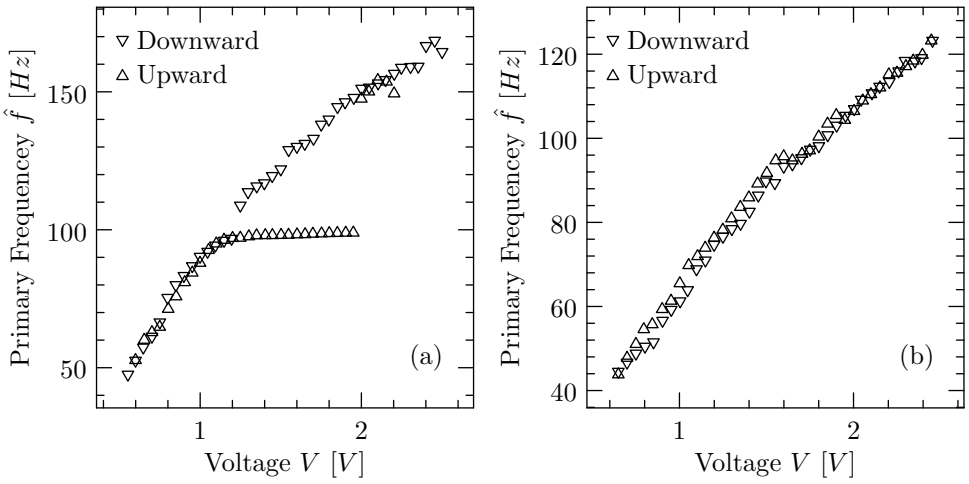

Figure 4.4: Frequency response of a single motor versus voltage, both (a) on a resonant plate, and (b) for comparison, a different motor on a rigid support.

The motor's primary frequency is relatively stable when the voltage is fixed, but figure 4.4(a) shows that the motor's frequency versus voltage[2] is hysteretic. Shown in figure 4.4(a) are the primary frequencies for two different sets of consecutive measurements, one in which I started at $V = 2.4\,V$ and slowly decreased the voltage to $0.6\,V$ (indicated by triangles pointing downward), and another in which I started the motors at $V = 0.6\,V$ and slowly increased the voltage to $2.4\,V$ (indicated by the triangles pointing upward). Although the two measurements demonstrate relatively good agreement below $V = 1\,V$ and above $V = 2\,V$, they exhibit a hysteresis between $V = 1V$ and $2\,V$. A motor on the lower branch gets stuck near a resonance of the plate and cannot reach the upper branch unless the driving voltage exceeds $V = 2\,V$. Once the motor reaches the upper branch, it does not drop to the lower branch unless the voltage drops below $V \approx 1.2\,V$, where it will remain unless the voltage is again increased above $V = 2\,V$. In contrast, similar data taken from a separate motor on a rigid support are shown in figure 4.4(b), showing that in the absence of resonances, a motor's frequency is nearly linear in the applied voltage. The marked difference indicates that the motor interacts strongly with the resonances of the plate, and these interactions lead to the

[2]Note that the primary frequency as a function of voltage in figure 4.4(a) is uncommonly high because this happens to be the fastest motor of the 16 included in this study. It is the same motor as the one operating between $f = 80\,Hz$ and $f = 95\,Hz$ between $V = 1.2\,V$ and $1.4\,V$ in figure 4.7(b).

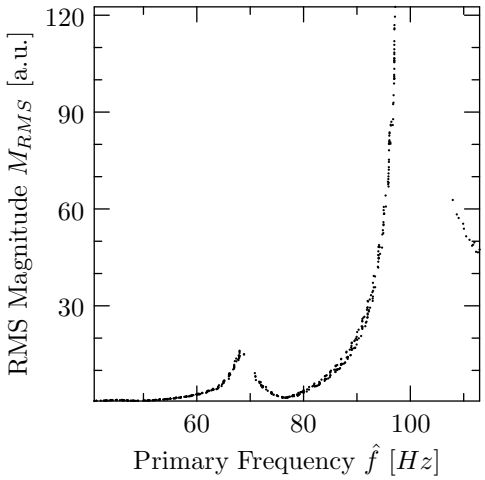

Figure 4.5: Accelerometer amplitude as a function of motor frequency when driven by a single motor. The peaks near 68 Hz and 97 Hz correspond with peaks in the support's Green function at the same frequencies.

hysteresis observed in figure 4.4(a).

I measure the magnitude of the plate's response using the root mean square (RMS) of the Fourier transform in the vicinity of the peak, M_{RMS}. I compute a number of estimates of the RMS magnitude, similar to the estimates for the primary frequency, as

$$M_{RMS,n} = \sqrt{\sum_{i=i_{peak}-n}^{i_{peak}+n} \frac{|\tilde{a}_i|^2}{T}}, \tag{4.3}$$

where T is the duration of the sample. For data in which the motor's frequency was indeed constant, the values obtained for $M_{RMS,n}$ are largely independent of n as long as the sum covers the extent of the peak. For a given sample, I assign $M_{RMS} = M_{RMS,20}$. The RMS magnitude can be plotted against the voltage V, but it is better understood as a function of the primary frequency $\hat{f}$, as shown in figure 4.5.

As shown in figure 4.5, the magnitude of the plate's response to a single motor is not monotonic in frequency. To understand this behavior, note that the plate has resonances near $68\,Hz$ and $100\,Hz$, so the plate will have larger accelerations when driven by a motor near these frequencies than when the motor's frequency is far from the resonances. These data were obtained by powering different motors—one at a time—at various voltages and taking

two-second data sets for each voltage. Although I could seek a relation between the RMS magnitude and the applied voltage, figure 4.5 indicates that the RMS magnitude is a function of primary frequency. Despite overlaying data from motors at various locations on the plate, the magnitude as a function of primary frequency is remarkably consistent, confirming that the coupling between the plate and the motors for this particular experimental setup does not depend substantially on the motor's position. Apart from the gaps in the data for frequencies just above the two peaks, which I discuss in the next section, the magnitudes in this plot are equivalent to $f^4\,|G|$, where G represents the passive frequency-dependent Green function of the system.

Spectroscopic observations and time-frequency plots indicate that a motor's primary frequency occasionally jumps quickly by one or two Hertz and then relaxes back to its pre-jump frequency over the next few seconds. The growth of $M_{RMS,n}$ as a function of n gives a simple criterion for identifying motor data in which the motor's frequency changes appreciably over the course of the sample. After examining many data samples, I decided to discard any data samples for which

$$\frac{M_{RMS,20}}{M_{RMS,1}} > 1.09. \tag{4.4}$$

In practice this amounts to rejecting about 10% of the samples.

All of the discussion of data presented so far has focused on single motors. Since I use a single accelerometer to measure the behavior of multiple motors acting simultaneously, and since I wish to know when two or more motors synchronize, I must obtain a reasonable estimate for the number of motors at a given frequency. Such an estimate is not trivial: the resonant response of the plate means that one motor turning at $95\,Hz$ will produce a much stronger signal than many synchronized motors with a primary frequency of $78\,Hz$. My solution to this problem is to use figure 4.5 as a normalization curve. I sample the RMS magnitude uniformly, interpolating where necessary, to obtain normalization amplitudes $\hat{M}\,(f)$. I then normalize a raw spectrum such as figure 4.3 by dividing the amplitudes of the

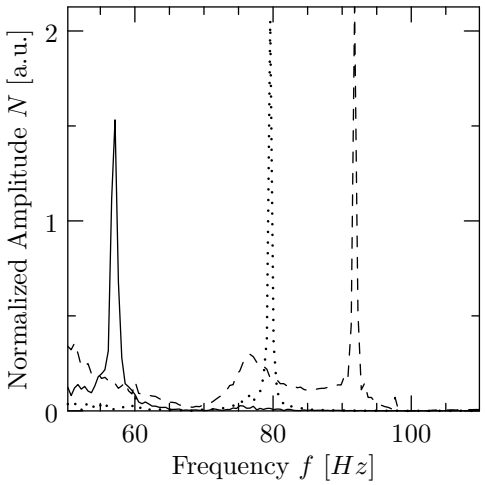

Figure 4.6: Normalized plot of data shown in figure 4.3. The driving voltages are $0.65\,V$ (—), $0.84\,V$ ($\cdots$), and $1.05\,V$ (- -).

original spectrum by the normalization amplitudes:

$$N(f) = \frac{|\tilde{a}(f)|}{\hat{M}(f)}. \tag{4.5}$$

The result of such a normalization scheme is shown in figure 4.6 for the data presented in figure 4.3. Except for the artifacts at $f = 50\,Hz$ and $75\,Hz$ associated with the signal at $V = 1.05\,V$, the scheme appears to work quite well. Even with the artifacts, single motors can be easily distinguished and counted, providing a decent measure of the number of motors in the vicinity of a given frequency.

4.3 Many Motors on a Resonant Plate

The behavior of multiple motors interacting on a plate is richer than the behavior of a single motor on a plate. In this section I explore that richness, first by examining how the driving voltage effects the behavior of the motors, and then by considering the non-transient behavior of the system at fixed voltage over long times.

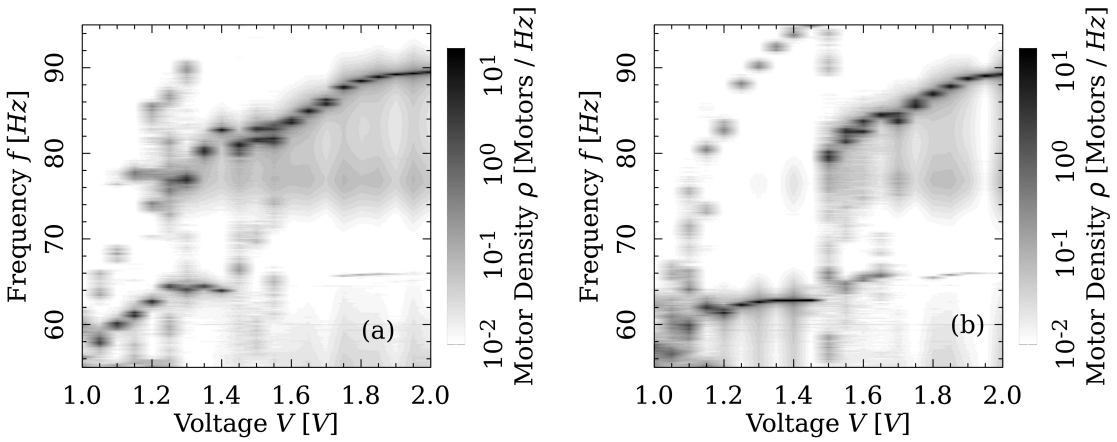

Figure 4.7: Behavior of many motors on a plate as a function of voltage. (a) Behavior as I decrease the voltage starting from an initially high value. (b) Behavior as I increase the voltage from an initially low value. The gray-scale is logarithmic in motor density.

Behavior versus Voltage

The essential behavior of multiple motors interacting on the plate is given in figure 4.7. These plots are consecutive minute-long measurements that have been Fourier transformed and normalized as discussed in the previous section, where I now identify the motor density ρ with the normalized amplitude:

$$\rho_V(f) = N(f, V). \tag{4.6}$$

Instead of plotting individual spectra, like those in figure 4.6, I plot consecutive spectra by creating gray-scale columns and laying them out sequentially in order of applied voltage. (This is similar to the greyscale plots introduced in Chapter 2, except that the probabilities are based on Fourier transforms instead of simple counts.) The difference between figures 4.7(a) and 4.7(b) is that in the former I started the system at high voltage and stepped the voltage down each consecutive measurement, whereas in the latter I started the system at low voltage and stepped the voltage up each consecutive measurement, in a manner similar to the data shown in figure 4.4.

The motors exhibit a number of consistent and contrasting behaviors between figures 4.7(a) and 4.7(b). Both figures indicate that for high voltages ($V > 1.7\,V$) the motors show strong

synchronization approaching $f = 90\,Hz$, and ensembles of motors near $f = 64\,Hz$ between $V = 1.2\,V$ and $1.4\,V$ maintain nearly the same frequency. Both figures also show almost no motor activity between $f = 65\,Hz$ and $75\,Hz$. The motors' behavior in the vicinity of the resonance near $f = 68\,Hz$ is the key difference between the figures. As with the single-motor data shown in figure 4.4, the motors show hysteresis behavior. Starting from low frequencies and moving upward—figure 4.7(b)—most of the motors synchronize strongly just below the resonance. The transition out of this synchronized state occurs swiftly and can be observed without any special equipment: the noise of the plate drops many decibels in less than a second. Once the motors have jumped above the $f = 68\,Hz$ resonance at $V = 1.5\,V$, many of them remain above that resonance in a less synchronized state despite reducing the voltage, as in figure 4.7(a), until the driving voltage drops below $V = 1.2\,V$.

The frequency of the resonance that causes the hysteresis is surprising and is due to interactions of multiple motors. Although the magnitude measurements in figure 4.5 clearly show the resonance near $f = 68\,Hz$, and seem to indicate a gap between $f = 68\,Hz$ and $71\,Hz$, the individual motor's behavior shown in figure 4.4(a) indicates that the resonance has no noticeable effect on the motor's frequency as a function of voltage. Yet, the same resonance has a substantial impact on the dynamics of the multi-motor system. The pronounced effect of the resonance in figures 4.7(a) and (b), and the lack of any effect in figure 4.4(a), suggest that a resonance's effect on a motor's steady-state frequency depends on the number of motors near the resonance. I have two additional observations that confirm this assertion.

I originally planned to study how the motors negotiated the strong resonance near $f = 100\,Hz$. The fastest motor, as reported in figure 4.5, jumps over the resonance at about $V = 2\,V$, but I do not observe any such transition for the same motor when operating all 16 motors even up to $V = 2.5\,V$. I do not drive the system much higher than $V = 2.5\,V$ for fear of tripping the power supply's fuse, and because my motors begin to degrade at such high voltages. Although I do not know the voltage at which the fastest motor would have negotiated the resonance, I do know that the effect of the resonance on the motor's steady

state behavior is different with other motors present than with the motor interacting with the plate alone.

I am also able to strengthen or weaken the stability of the group of oscillators synchronized near $f = 64\,Hz$ by changing the behavior of a single motor. Note that in figure 4.7(b) at $V = 1.15\,V$, there is a motor turning with frequency $f = 74\,Hz$. Before proceeding to $1.2\,V$, I forced the motor back down to the ensemble near $62\,Hz$, with which it remained synchronized until the transition at $V = 1.5\,V$. Had I continued the measurements with that motor left unchecked, as I did in other measurements, the synchronization at $63\,Hz$ would have dispersed at $V = 1.35\,V$. Forcing the motor in question to operate at the lower frequency may have strengthened the synchronization of that group of motors, or alternatively, the presence of the motor operating at the higher frequency may have weakened the synchronization of that group of motors. I cannot say which of these explanations is correct, but I can confirm that the interaction of the motors with the resonance can change substantially by changing the behavior of one of the motors.

The motors avoid frequencies between $f = 65\,Hz$ and $75\,Hz$. From my experience with the Kuramoto model, I had expected the motors' frequencies to continuously increase through a resonance as I increased the driving voltage, but the empty region between $f = 65\,Hz$ and $75\,Hz$ in figures 4.7(a) and (b) as well as the gaps above the resonances in figure 4.5 indicate that the motors avoid those frequencies when approaching from both below and above the resonance. This is an important effect that I will explore further in the next Chapter.

The RMS magnitude shown in figure 4.5 measures how strongly the plate couples with the motor and conversely how strongly a motor couples with a vibrating plate. If two or more motors are running simultaneously on the plate, this should also give some indication for how strongly they will interact with each other, making it a proxy for the frequency-dependent coupling between motors due to the plate. A rudimentary prediction of standard models of coupled oscillators [9] is that the effective distribution of the oscillators' frequencies narrows as the coupling between them increases. If the RMS magnitude is a good proxy

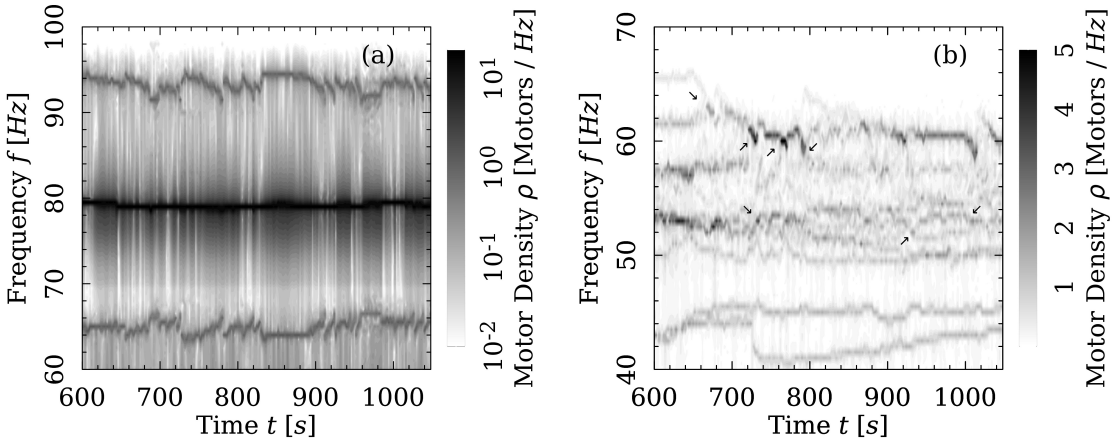

Figure 4.8: Normalized spectrograms of dynamics of multiple motors on a resonant plate. (a) Behavior at $1.49\,V$, using a logarithmic gray-scale. (b) Behavior at $1.06\,V$, using a linear gray-scale. The arrows in figure (b) indicate synchronization or desynchronization events.

for the coupling strength, then the narrow frequency distributions in figures 4.7(a) and (b) should correspond to frequencies with greater RMS magnitudes. The narrowest frequency distributions correspond to frequencies close to $f = 63\,Hz$ and close to $f = 88\,Hz$ or greater, and the most dispersed frequency distributions correspond to frequencies near $f = 80\,Hz$ or below $f = 60\,Hz$. These frequencies respectively correspond with the greatest and least values of M_{RMS}, as reported in figure 4.5.

Behavior versus Time

The spectrograms in figures 4.8 give an alternate perspective on the motors' behavior. These figures show the non-transient dynamics of the motors at a fixed voltage over about eight minutes. The plots have been prepared by dividing their associated time series into two-second intervals, Fourier Transforming the data in each interval, normalizing the data by dividing as explained in the previous section, and plotting consecutive columns. Both systems were given at least 10 minutes to adjust to their stated voltages before these data were taken, so the results represent the non-transient behavior of the system. The differences between figure 4.8(a) and 4.8(b) is that in the former the operating voltage is $V = 1.49\,V$ and the

gray-scale is logarithmic in motor density, whereas in the latter the operating voltage is $V = 1.06\,V$ and the gray-scale is linear in motor density. In figure 4.8(a), 14 of the motors synchronize near $f = 79\,Hz$ while one motor turns near $f = 65\,Hz$ and another turns near $f = 93\,Hz$. In figure 4.8(b), all of the motors operate between $f = 40\,Hz$ and $60\,Hz$, synchronizing in small groups, and spontaneously desynchronizing.

A striking feature of figure 4.8(a) is the apparent mirror symmetry. The fourteen motors synchronized at $f = 79\,Hz$ vary within less than $1\,Hz$, appearing essentially flat, while the much larger fluctuations of the two other motors are negatively correlated. The slower motor is roughly $\Delta f = 14\,Hz$ below the synchronized group, while the faster motor is equally far above the group. The magnitudes of the changes are nearly identical: for example, both motors' frequencies jump by $\Delta f = 2\,Hz$ at $t = 780\,s$. The symmetric behavior of the two motors is reproducible[3] for voltages in the range $1.48\,V < V < 1.52V$. The mirror symmetry suggests that the overall average frequency of all 16 motors is a conserved quantity for non-transient behavior.

Despite the stark contrast between data plotted in figures 4.8, the second figure also demonstrates behavior that supports my tentative hypothesis that the average frequency is constant. However, the evidence is more subtle and focuses on details of synchronization and desynchronization events. Consider a subset of the motors which transition from two small synchronized groups to one larger synchronized group. If the other motors in the system maintain relatively constant frequencies, then the hypothesis of constant average frequency would imply that the average frequency of the subset would be constant. Furthermore, the slopes of the small groups as they approach each other must satisfy $N_i \frac{df_i}{dt} + N_j \frac{df_j}{dt} = 0$. These criteria appear to be satisfied by many synchronization and desynchronization events in figure 4.8(b) as indicated by the arrows in the figure. The simplest synchronization event occurs at the beginning of the time-series, $t = 600\,s$. Two motors are synchronized at

[3]In addition, the system must be prepared such that the slowest motor is below resonance and the fastest motor is not synchronized, which can be difficult since the system's state is not a function of the driving voltage.

$f_2 = 61.5\,Hz$ and a third turns at $f_1 = 65.5\,Hz$ giving an average of $\bar{f} = 62.8\,Hz$; when these three motors synchronize briefly at $t = 670\,s$, their synchronized frequency is between $f_{sync} = 62.5\,Hz$ and $63\,Hz$, agreeing well with the prediction. For the pair of motors just before synchronization, $\frac{df}{dt} = 0.0714\frac{Hz}{s}$, and for the top motor just before synchronization, $\frac{df}{dt} = -0.125\frac{Hz}{s}$, nearly twice the magnitude and opposite sign. Unfortunately, the data for the noted synchronization and desynchronization events are imprecise and do not definitively establish my hypothesis for average frequency conservation.

I conclude this section by drawing attention to the many time scales exhibited in figures 4.8(a) and (b). The motors occasionally exhibit long durations of stability, such as the slowest motor in figure 4.8(a) from $t = 840\,s$ to $880\,s$, and the fastest motors in figure 4.8(b) from $t = 950\,s$ to $990\,s$. Both figures exhibit jumps in motor frequency, and the magnitude of the jumps as well as the decay-like response that follows involve time scales whose origins are not apparent in the data. I do not have an explanation for these time scales and a full analysis will have to wait for more detailed measurements.

4.4 Conclusion

I find that the behavior of individual motors and ensembles of motors interacting with a resonant plate shows a characteristic signature near the resonances of the plate. Motors interacting with a resonance tend to avoid frequencies just greater than the resonant frequency; operating frequencies level-off just below a resonance; and the stability of a collection of motors near a resonance is not the same as the stability of a single motor near a resonance. These characteristics have the overall effect of creating a hysteresis in frequency versus voltage both for a single motor on the plate and for a collection of motors. Once all of the transient behavior has passed, I find evidence that the average motor frequency is constant.

All of these observations provide useful criteria for developing models of frequency-dependent coupling in systems of many coupled oscillators, which I consider next.

Chapter 5

Modeling Resonant Coupling

The previous Chapter concluded with a set of general properties that a model of the motors must demonstrate. In this Chapter I develop a model that satisfies most of those properties. Although it can be made to look suspiciously like the Kuramoto model, I derive it from a first principles analysis of the motor dynamics.

The behavior of the motors I obtain in this Chapter closely resembles the Kuramoto model, but the differences are important. In particular, the coupling is a function of the motors' frequencies, and the resonant coupling introduces a frequency-dependent phase delay.

5.1 Basic Model

Figure 5.1 shows a schematic of one of the eccentrically weighted dc motors that I use in my laboratory and describes an idealized mechanical model for the dynamics of the ith such

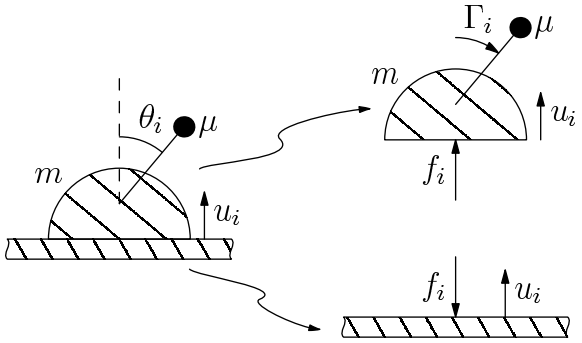

Figure 5.1: Motor illustration. The mechanical model describes an eccentrically weighted DC motor on a compliant foundation. The motor has total mas $m + \mu$. It has a rotor of mass μ, first moment of inertia λ, and second moment of inertia I. The rotor is subject to an applied torque Γ_i and a viscous drag (not illustrated).

motor in terms of its orientation $\theta_i(t)$ and the displacement $u_i(t)$ of the support under it. A force $f_i(t)$ acts upwards on the motor and downwards on the support. The rotor is taken to have moment of inertia I around its axis, first moment of mass λ, and total mass μ. The rest of the motor has mass m. A torque Γ is applied to the rotor by the motor, controlled by the current supplied to the motor. I neglect horizontal forces in this analysis because the support is stiff against horizontal motions. In other words, the support's side-to-side motion is negligible. I take as the governing equations Newton's second law for forces and torques. The torque equation reads

$$I\frac{d^2\theta_i}{dt^2} = \Gamma_i - \alpha\frac{d\theta_i}{dt} + \lambda\sin\theta_i\frac{d^2u_i}{dt^2}, \tag{5.1}$$

where I model the motor's drag with a viscous coefficient α and the last term is a fictitious torque due to the motor's accelerating reference frame. In this work I will ignore gravity, which means that each motor has only one force: the force of the plate on the motor. However, the mass term is complex and force balance gives

$$f_i = (m+\mu)\frac{d^2u_i}{dt^2} + \lambda\frac{d^2\cos\theta_i}{dt^2}. \tag{5.2}$$

For linear systems such as the support, the displacements u_i at one location and time can be expressed as a convolution of a Green function with the forces f_j applied at other points and times. Using this formalism, I close the system of equations 5.1 and 5.2 by writing

$$u_i = -\sum_j G_{ij} \otimes f_j, \tag{5.3}$$

where $\otimes$ represents a temporal convolution and G_{ij} is the Green function for the support. The minus sign arises from the oppositely defined direction for f and u. Furthermore, I introduce an ancillary Green function g_{ij}, defined most readily in abstract terms and direct matrix notation:

$$\mathbf{g} = \left[\mathbf{G}^{-1} + (m+\mu)\,\mathbf{I}\frac{d^2}{dt^2}\right]^{-1}. \tag{5.4}$$

$\mathbf{g}$ may be interpreted as Green's function for the structure with added point masses $m+\mu$ at the positions of all the motors. Here $\mathbf{I}$ is the identity matrix.

The experimental system I aim to model is a resonant support, for which $\mathbf{g}$ will be best represented in its modal expansion. It is often convenient to represent $\mathbf{g}(t)$ and its Fourier Transform $\tilde{\mathbf{g}}(\omega)$ as a sum over natural modes r:

$$g_{ij}(t) = \sum_r g^r(t)\, u_i^r u_j^r, \tag{5.5}$$

$$\tilde{g}_{ij}(\omega) = \sum_r \tilde{g}^r(\omega)\, u_i^r u_j^r. \tag{5.6}$$

Each resonance has a frequency ω_r, modal mass M_r, and decay time T_r. Here u_i^r is the rth resonance's displacement amplitude (not $u_i(t)$) at the position of the ith motor. I relate the decay times to the resonant frequencies by the (unitless) loss tangent $\eta_r \equiv (\omega_r T_r)^{-1}$, allowing me to express the Green function from a single resonances as:

$$g^r(t) = \sin(\omega_r t)\, \frac{e^{-\eta_r \omega_r t}}{M_r \omega_r}, \tag{5.7}$$

$$\tilde{g}^r(\omega) = \int_0^\infty g_{ij}(t)\, e^{\imath\,\omega\, t} dt = \frac{M_r^{-1}}{(\eta_r \omega_r - \imath\,\omega)^2 + \omega_r^2}. \tag{5.8}$$

$\tilde{g}^r$ represents the Fourier transform of the resonance and $\imath = \sqrt{-1}$. I will also sometimes make use of the magnitude and phase of the Fourier transform of the Green function or its resonances:

$$\tilde{g}_{ij}(\omega) \equiv |\tilde{g}_{ij}(\omega)|\, e^{\imath\,\gamma_{ij}(\omega)}, \tag{5.9}$$

$$\tilde{g}^r_{ij}(\omega) \equiv \left|\tilde{g}^r_{ij}(\omega)\right| e^{\imath\,\gamma^r_{ij}(\omega)}. \tag{5.10}$$

I use $\mathbf{g}$ to combine equation 5.1 and 5.2 and eliminate the variables f and u, obtaining a set of integro-differential equations for the θ:

$$I\frac{d^2\theta_i}{dt^2} = \Gamma_i - \alpha\frac{d\theta_i}{dt} + \lambda \sin\theta_i \sum_j \frac{d^2}{dt^2}\left[g_{ij} \otimes \left(-\lambda \frac{d^2 \cos\theta_j}{dt^2}\right)\right]. \tag{5.11}$$

In the absence of coupling (e.g. set λ to zero) each motor achieves a steady state at $\theta_i = \omega_i\, t + \theta_{i0}$ with a natural speed $\omega_i = \Gamma_i/\alpha$ and an arbitrary phase θ_{i0}. After a brief transient, the motors usually reach roughly constant velocities, so I neglect the second time derivative

on the left to simplify the governing equation:

$$\frac{d\theta_i}{dt} = \omega_i - \frac{\lambda^2}{\alpha} \sin\theta_i \sum_j \frac{d^2}{dt^2} \left[g_{ij} \otimes \left(\frac{d^2 \cos\theta_j}{dt^2} \right) \right]. \tag{5.12}$$

It is for this integro-differential equation that I will seek analytic and numeric solutions.

5.2 Analytic solutions

Without loss of generality I set $\theta_i(t) = \Omega t + \phi_i(t)$ with Ω to be determined:

$$\frac{d\phi_i}{dt} = \omega_i - \Omega - \frac{\lambda^2}{\alpha} \sin(\Omega t + \phi_i) \sum_j \frac{d^2}{dt^2} \left[g_{ij} \otimes \frac{d^2 \cos(\Omega t + \phi_j)}{dt^2} \right]. \tag{5.13}$$

I now apply a series of approximations to derive an expression that can be more easily interpreted. If the ϕ vary slowly, as they will if every motor has a speed at or close to Ω, then the effect of $\mathbf{g}$ can be approximated well in the frequency-domain in terms of a transfer function $|\tilde{g}_{ij}(\Omega)|$ and a phase delay $\gamma_{ij}(\Omega)$, as in equation 5.9. Similarly each pair of time derivatives is well approximated by a factor of $-\Omega^2$:

$$\frac{d\phi_i}{dt} = \omega_i - \Omega - \frac{\lambda^2 \Omega^4}{\alpha} \sin(\Omega t + \phi_i) \sum_j |\tilde{g}_{ij}(\Omega)| \cos\big(\Omega t + \phi_j - \gamma_{ij}(\Omega)\big). \tag{5.14}$$

Using a trigonometric identity, I combine the sine and cosine terms on the right side, leading to a rapidly varying part (at frequency 2Ω) and a slowly varying part. I eliminate the rapidly varying part by averaging over one cycle, giving

$$\frac{d\phi_i}{dt} = \omega_i - \Omega - \frac{\lambda^2 \Omega^4}{2\alpha} \sum_j |\tilde{g}_{ij}(\Omega)| \sin\big(\phi_i - \phi_j + \gamma_{ij}(\Omega)\big). \tag{5.15}$$

Each of the diagonal elements of the Green function of a dissipative structure must have a positive imaginary part[1], i.e. $\sin\gamma_{ii} \geq 0$, so I restrict my attention to $0 \leq \gamma_{ii} \leq \pi$.

If I ignore the i, j, and Ω dependence in $\mathbf{g}$ and if the γ_{ij} are zero, I recover the Kuramoto model. Sakaguchi and Kuramoto [14] considered the effect of a constant, uniform phase delay

[1] Supports of physical interest lose energy to heat and acoustic radiation. This energy must come from the motors, which requires that velocity responses be in phase with the forcing.

$\gamma_{ij} \equiv \gamma$ and Yeung and Strogatz considered explicit time delays [44]. To my knowledge no-one has examined Ω dependence. In the case of a highly resonant support, $\eta \ll 1$, Ω dependence can be strong.

Synchronization in the above system is complex. To better understand how the system behaves, I will analyze some special cases. I will begin by assuming all the motors are identical, $\omega_i = \omega$ for all i. I furthermore require all motors to be coupled identically, independent of i and j, a condition that applies to the experimental setup in the last Chapter. Thus $g_{ij}(\Omega) = g(\Omega)$, $\gamma_{ij}(\Omega) = \gamma(\Omega)$, and I have

$$\frac{d\phi_i}{dt} = \omega - \Omega - \frac{\lambda^2 \Omega^4}{2\alpha} \sum_j |g(\Omega)| \sin\left(\phi_i - \phi_j + \gamma(\Omega)\right). \tag{5.16}$$

The synchronized state is now easy to identify; it corresponds to $\phi_i = 0$ for all i, and requires

$$\begin{aligned} \Omega &= \omega - \frac{N\lambda^2 \Omega^4}{2\alpha} |\tilde{g}| \sin\gamma \\ &= \omega - \frac{N\lambda^2 \Omega^4}{2\alpha} \Im\{\tilde{g}(\Omega)\} \end{aligned} \tag{5.17}$$

In this state, all motors have identical phases and run at speed Ω diminished from their natural speed ω by an amount that scales with N and with the positive quantity $|g| \sin\gamma$. The acoustic power output of the N motors is the difference between the rate of work done by the torques Γ and the loss in the viscous mechanisms, i.e.

$$N\left(\Gamma\Omega - \alpha\Omega^2\right) = N\Omega\alpha(\omega - \Omega) \tag{5.18}$$

$$= \frac{1}{2} N^2 \lambda^2 \Omega^5 |g| \sin\gamma. \tag{5.19}$$

Inasmuch as this scales with the square of the number of motors, the system exhibits stimulated emission and super radiance. By linearizing equation 5.16 around the synchronized state $\phi_i = 0$ for all i, it is not hard to show that the synchronized state is stable against all infinitesimal perturbations (except the trivial marginally stable perturbation of a uniform shift of all ϕ) if and only if the real part of the Green function is positive, i.e. $\cos\gamma > 0$.

Another solution to equation 5.16 is apparent, in which the θ are distributed uniformly between 0 and $2\,\pi$:

$$\theta_i = \omega\, t + \frac{2\,\pi\, i}{N}, \tag{5.20}$$

for a suitable ordering of the θ_i. This state has $N-2$ neutrally stable linear perturbations. The two remaining perturbations exhibit time-dependence proportional to $e^{\nu\, t}$ with

$$\nu = N\frac{\lambda^2\,\omega^4}{4\,\alpha} e^{\pm\imath\,\gamma}\left|\tilde{g}\left(\gamma\right)\right|. \tag{5.21}$$

On the stiffness controlled, low frequency side of a resonance, where $0 < \gamma < \pi$, these dispersed states are unstable. On the mass controlled high-frequency side of a resonance, the Green function has a negative real part (i.e. $\frac{\pi}{2} < \gamma < \pi$), making the modes exponentially stable.

Figure 5.2 plots the solution $\Omega\left(\omega\right)$ to equation 5.17 for the case of a single resonance (the sum over r in equation 5.6 has one term). I plot

$$\Omega = \omega - \frac{M_r\, X\, \Omega^4}{2}\Im\left\{\tilde{g}^r\left(\Omega\right)\right\} \tag{5.22}$$

$$= \omega - X\frac{\eta_r\,\omega_r\,\Omega^5}{\left(2\,\eta_r\,\omega_r\,\Omega\right)^2 + \left(\omega_r^2 - \Omega^2 + \eta_r^2\,\omega_r^2\right)^2}, \tag{5.23}$$

where I have introduced a coupling strength parameter $X = N\,\lambda^2/\left(\alpha\, M_r\right)$. The coupling strength is measured in units of seconds per radian.

For a single resonance, the stability criterion $\cos\gamma > 0$ only holds for $\Omega < \omega_r\sqrt{1+\eta_r^2}$. Thus by this theory I expect to see no synchronization at speeds Ω on the mass controlled, high frequency, side of a resonance, regardless of the driving torques and the natural motor speeds ω. Solutions to equation 5.23 that satisfy this criterion follow the bold lines in the figure. The nearly flat regions for the synchronized speed Ω in the vicinity of $0.075\,\mathrm{rad/s}$ correspond to the speed of the synchronized state being almost independent of torque. For very high driving torque, however, the synchronized state loses its stability.

Figure 5.3 shows a plot for the more complex case of two resonances. Each resonance gives rise to a range of natural speeds ω for which the synchronization speed Ω is slightly

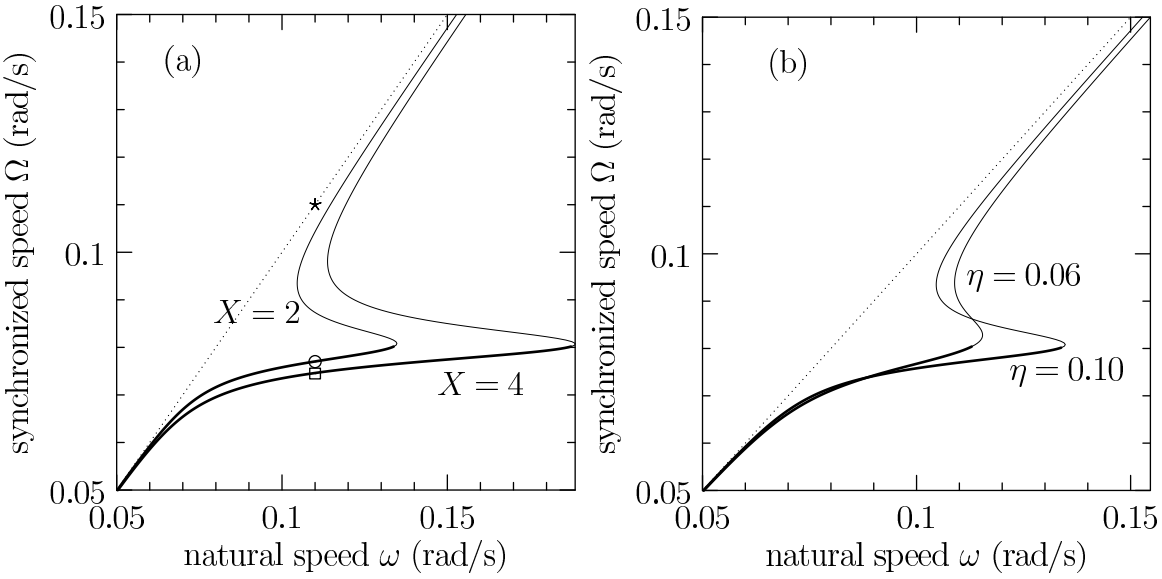

Figure 5.2: Representative cases for Ω, the speed of the synchronized state, as a function of the natural speeds ω of the motors, according to equation 5.23. The bold lines are the solutions that I expect to be stable because the imaginary part of $\tilde{\mathbf{g}}$ is positive. The thin lines are solutions for which the imaginary part of $\tilde{\mathbf{g}}$ is negative, and should be unobservable in practice. The dotted line $\Omega = \omega$ is provided for reference. For all four curves, the resonant frequency ω_r is 0.08 rad/s. Figure (a) shows curves for two different couplings X and the same loss tangent η of 0.06. Figure (b) shows curves for two different loss tangents η but identical coupling $X = 2\,\mathrm{s/rad}$. The star, circle, and square in figure (a) are related to figures 5.4 and 5.5, and are discussed in section 5.3.

less than a resonance frequency and nearly independent of the natural speed. These ranges overlap for the two resonances, leading to a regime—ω between 0.08 and 0.11 rad/s—in which the system can synchronize at either of two speeds Ω. Furthermore the system cannot synchronize over a range of Ω from 0.06 to 0.075 rad/s. All of these satisfy the criteria stated in the previous Chapter, and arise in my numerics in the next section, even those involving disorder.

5.3 Numerical solutions

The experiments that motivated this model have disorder in the sense that natural motor speeds vary amongst the motors. Such a generalization does not readily lend itself to the

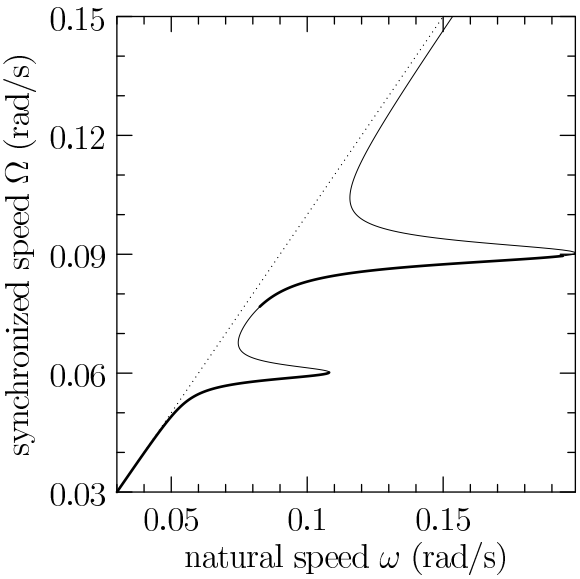

Figure 5.3: The solution to equation 5.17 for the case in which the Green function $\mathbf{g}$ has two resonances. For the meaning of the line weights, see figure 5.2. The resonances have identical coupling strengths X_1 and X_2 of 2.0 s/rad and identical loss tangents η_1 and η_2 of 0.038, but different resonant frequencies: $\omega_1 = 0.06\,\mathrm{rad/s}$, $\omega_2 = 0.09\,\mathrm{rad/s}$.

analysis of section 5.2. Nor does the above analysis shed much light on the dynamics: how does the system approach the stable synchronized state? Nor does it shed light on errors that may have been introduced by the short time averaging used to eliminate the terms in $2\,\Omega$. For all those reasons, I now turn to numerical solutions.

I examine numerical solutions of the integro-differential equation 5.12 for their correspondence to the simple model discussed in section 5.2 and my previous laboratory observations. I rewrite equation 5.12 using a modal expansion for the Green function:

$$\frac{d\theta_i}{dt} = \omega_i - \frac{1}{N}\sin\theta_i \sum_{r,\,j} \frac{d^2}{dt^2}\left(X_r\, h^r \otimes \frac{d^2\cos\theta_j}{dt^2}\right) \tag{5.24}$$

where I take the ancillary green function for each resonance h^r in the form

$$h^r(\tau) = \sin(\omega_r\,\tau)\,\frac{e^{-\eta\,\omega_r\,\tau}}{\omega_r}. \tag{5.25}$$

I label resonances by r and factors of λ^2, α, and M have been absorbed into the coupling strengths X_r, as in the previous section.

Numerical solutions of equation 5.24 are of necessity approximate. I employ a simple Euler tangent approximation for the first time derivative, and evaluate the convolution by discrete integrations and the second time derivatives by discrete differencing. I define my units such that a single time step is one second. I choose motor speeds of about 0.1 rad/s, meaning the motors advance their phases by about 0.1 rad each time step. The scheme is prohibitively implicit if these second derivatives are evaluated centrally; they are therefore evaluated with a delay of one time step. While the resulting time series will differ from exact solutions of the original equations, I expect the qualitative behavior to be correct. All studies are for $N = 100$.

In the previous section, Ω denoted the speed at which the motors synchronized. Since that population of motors had no disorder, the synchronized speed was identical to the average speed. I will consider populations with disorder in this section, and I will redefine Ω as the average motor speed:

$$\Omega = \frac{1}{N} \sum_i \dot{\theta}_i. \tag{5.26}$$

Approach to the steady-state

I first evaluate how the system evolves from random initial conditions. The simulations typically achieve a steady state after about 2000 seconds. Figures 5.4 to 5.6 show the evolution of the speeds (averaged over 16 time steps) of 11 arbitrarily chosen motors. They also show the evolution of an order parameter defined as

$$R = \frac{1}{N} \left| \sum_i e^{\imath \theta_i} \right|. \tag{5.27}$$

This order parameter is identical to the standard Kuramoto order parameter: if the motors are in phase, R will be close to 1, if they are uniformly distributed between 0 and 2π, R will be close to 0, and if the motors have random phases, R will exhibit random fluctuations about an RMS of $N^{-1/2} = 0.1$. The resonant frequency ω_r is the same among all three figures (0.08 rad/s) and the loss tangent η is the same (0.06). The figures differ only in their

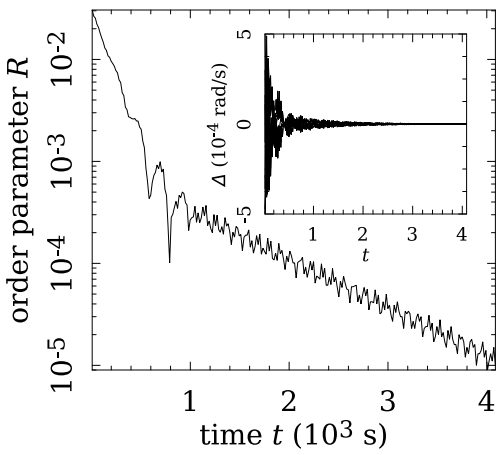

Figure 5.4: Order parameter R and discrepancy $\Delta_i \equiv \dot{\theta}_i - \omega$ between instantaneous motor speeds and the natural motor speed, for 100 identical motors. The initial phases were distributed randomly. For these plots, the natural speed of the motors ω was 0.11 rad/s. There was a single resonance with frequency ω_r of 0.08 rad/s, loss tangent η of 0.06, and coupling strength X of 2 s/rad. The subfigure shows how the instantaneous speeds differ from the natural speed of 0.11 rad/s, for 11 arbitrarily chosen motors. The final state corresponds to the star in figure 5.2(a).

coupling strengths X and the presence or absence of quenched disorder amongst the motors' natural speeds.

In the simulation shown in figure 5.4, the motors settle at their natural speed of 0.11 rad/s. According to equation 5.23 (and indicated by the open circle in figure 5.2), there is a synchronized speed Ω of 0.075 rad/s. The motors do not choose that solution, even when slight noise is artificially introduced. The motors settle instead into a state, indicated in figure 5.2 by a star, in which each motor runs at close to its natural speed. The order parameter decreases exponentially, which agrees with the previous section's prediction of exponential stability of the uniformly distributed state. In other simulations, with different initial conditions, I was able to obtain synchronized behavior with mean speed Ω that matched the prediction of 0.075 rad/s. Thus both the synchronized and the uniformly distributed states are stable, as predicted.

The behavior changes substantially at a greater coupling strength of $X = 4$ s/rad, as shown in figure 5.5. After a transient, the motors synchronize at a speed of $\Omega = 0.073$ rad/s

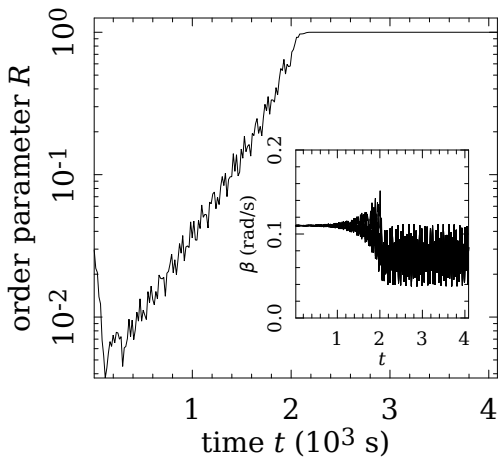

Figure 5.5: Order parameter R and representative speeds $\beta_i \equiv \dot{\theta}_i$ for a simulation of 100 identical motors with initial phases distributed randomly. In contrast to figure 5.4, the coupling strength X of the resonance was 4 s/rad; all other parameters were identical. The final state corresponds to the open square in figure 5.2(a).

and an order parameter of unity. The late time behavior shows a residual oscillation at a rate $2\,\Omega$, neglected in deriving equation 5.17. The open box in figure 5.2 is the corresponding prediction, a speed of $\Omega = 0.0745\,\mathrm{rad/s}$. The discrepancy may be due to numerical imprecision in computing Ω from the data in figure 5.5; it may be because the neglected oscillations at speed $2\,\Omega$ are indeed significant; it may be due to the discretization in the implementation of the numerics. Whatever the source of the discrepancy, it is small and the decision to neglect fluctuations of frequency $2\,\Omega$ in deriving equation 5.16 appears justified.

Figure 5.6 shows a case of disorder in the distribution of motor speeds. By introducing a Gaussian distribution of natural motor speeds with a standard deviation of 10% (i.e. $\bar{\omega} = 0.1\,\mathrm{rad/s}$ and $\sigma = 0.01\,\mathrm{rad/s}$), I find that a few of the motors have left the pack and the order parameter is reduced below unity. Like the motor behavior presented in figures 5.4 and 5.5, the motors in figure 5.6 approach their steady state behavior exponentially and in about 15 cycles. These compare favorably with observations from the laboratory, in which transient behavior was so fast that it was not measurable.

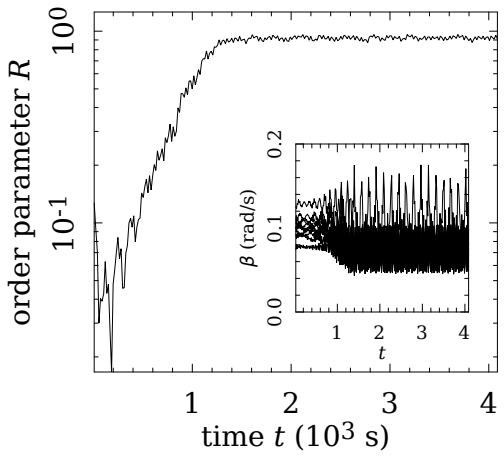

Figure 5.6: Order parameter R and representative motor speeds $\beta_i \equiv \dot{\theta}_i$ for a disordered population of 100 motors, started from initially random phases. The resonance parameters were the same as in figure 5.4, except the coupling X was 2.9 rad/s. The natural frequencies were chosen from a Gaussian distribution with mean $\bar{\omega}$ of 0.1 rad/s and standard deviation σ of 0.01 rad/s (i.e. 10% of $\bar{\omega}$).

Numerical solutions for swept natural motor speeds

In the laboratory observations presented in Chapter 4, I monitored behavior as a function of driving voltage, which determines torques and thus serves as a proxy for mean natural motor speed. The voltage was slowly swept, in a stepwise fashion, from a low to a high or a high to a low value, giving the motors time to adjust at each value. The laboratory system had two resonances and was noteworthy for a parameter regime in which the system could synchronize at either of two distinct frequencies. Each such frequency was slightly below one of the plate's resonant frequencies. Which frequency the system chose was a function of its history. It was also noteworthy for its observation of a spectral gap, a frequency range between the resonant frequencies in which the system was never seen to oscillate coherently. As discussed above the analytic solutions shown in figure 5.3 obey these criteria.

Birythmic hysteresis and a spectral gap are behaviors seen in the numerics also. I ran numerical simulations for the integro-differential equations

$$\frac{d\theta_i}{dt} = \omega_i - \frac{1}{N}\sin\theta_i \sum_j \frac{d^2}{dt^2}\left(h \otimes \frac{d^2\cos\theta_j}{dt^2}\right) \tag{5.28}$$

again with Green's function independent of i and j, but now corresponding to a set of motors on a support with two resonances:

$$h(\tau) = X_1 \sin(\omega_{r1}\,\tau)\,\frac{e^{-\eta_1\,\omega_{r1}\,\tau}}{\omega_{r1}} + X_2 \sin(\omega_{r2}\,\tau)\,\frac{e^{-\eta_2\,\omega_{r2}\,\tau}}{\omega_{r2}}. \tag{5.29}$$

Analytic predictions for this two-resonance structure are shown in figure 5.3.

The numerical simulations were performed in sweeps of 256 blocks. Mimicking the laboratory measurements, each block had three phases of 1024 seconds apiece: a sweep phase, a hold phase, and a measure phase. During the sweep phase, the natural speeds were slowly increased or decreased at a rate of $2^{-20} = 9.54 \times 10^{-7}\,\mathrm{rad/s^2}$. During the hold phase, the natural speeds were held fixed to allow transients to dissipate[2]. As such, the total number of time steps for a single upward or downward sweep was $256 \times 3 \times 1024$. During the measure phase, the natural speeds were again held fixed and I measured time series for the instantaneous speeds $\dot{\theta}_i$, order parameter R, and other data.

I ran cases in which every motor had identical natural motor speed ω_i and the results corresponded very closely to the predictions of section 5.2, in particular to the curves of figure 5.3. Figure 5.7 shows the mean motor speed Ω as a function of mean natural motor speed $\bar{\omega}$, for the case of disorder. For reference, I have included the stable solutions of figure 5.3. Natural motor speeds were taken randomly from a Gaussian distribution with a non-zero mean $\bar{\omega}$ and with a width of 5% or 10% of the mean for subfigures (a) and (b), respectively. I maintained the percentage width of the population throughout the simulations by stretching or compressing the population as I increased or decreased the mean natural motor speed $\bar{\omega}$.

The numerical and theoretical results plotted together in figure 5.7 agree nicely. The sweep of the solution of the coupled ordinary differential equations 5.24 reproduces much

[2]The hold phase is only 1024 seconds, which is shorter than the reported transient times in the previous subsection. However, those transient times are for a system starting from completely random initial conditions; the motors in the sweeps are not so disordered, and do not need so much time for their transient to diminish.

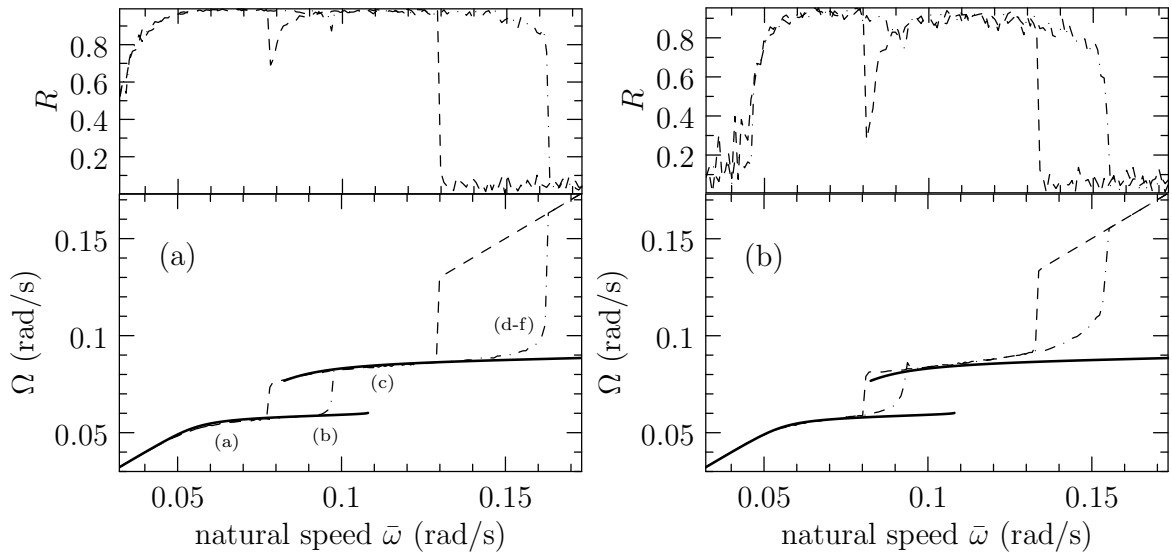

Figure 5.7: Order parameter R and average motor speeds Ω for sweeps of mean natural motor speed $\bar{\omega}$ from 0.03 to 0.2 rad/s (dash-dotted curves) and then back to 0.03 rad/s (dashed curves), for disordered populations. For figure (a), the standard deviation of the natural motor speeds ω_i is $\sigma = 0.05\,\bar{\omega}$, whereas for figure (b) it is $\sigma = 0.1\,\bar{\omega}$. These results correspond to $X_1 = X_2 = 2.0$ s/rad, $\omega_{1r} = 0.06$ rad/s, $\omega_{2r} = 0.09$ rad/s, $\eta_1 = \eta_2 = 0.038$. The solid curves indicate stable solutions for no disorder from equation 5.17 and plotted in figure 5.3. The marked locations in figure (a) correspond to spectral power densities of figure 5.8.

of the behavior predicted by the simpler analytic model of equation 5.17, and found also in the laboratory measurements in figure 4.7. I note in particular the birythmic hysteresis, the spectral gap, and the wide regions in $\bar{\omega}$ over which Ω is nearly constant at a value a bit less than ω_r. Neither disorder nor modeling of the fast time scales (ignored in section 5.2) have qualitatively changed these features.

Disorder has displaced and reduced some of the sharp features in $\Omega\,(\bar{\omega})$. Transitions in the order parameter remain sharp, suggesting that mean speed Ω fails to fully represent the state of the system. For that purpose, it may be better to address the chief interest for lasers: the spectral density of the wave power radiated by the oscillators.

Spectral power density and lasing transition

The energy radiated into the support by the motors can be written as a time-integral of force times velocity. The work done is

$$W = -\int \sum_i f_i(t) \frac{d}{dt} u_i(t)\, dt.$$

Expressing the displacements u_i in terms of the forcing f_i and the Green function $\mathbf{G}$, and using Parseval's identity, I can rewrite the above equation as

$$W = \frac{-1}{2\pi} \int \imath\, \omega \sum_{i,j} \tilde{f}_i^*(\omega)\, \tilde{G}_{ij}(\omega)\, \tilde{f}_j(\omega)\, d\omega \tag{5.30}$$

$$= \frac{-1}{2\pi} \int \omega\, \imath\, \omega \sum_{i,j} \tilde{q}_i^*(\omega)\, \tilde{g}_{ij}(\omega)\, \tilde{q}_j(\omega)\, d\omega \tag{5.31}$$

where

$$q_i(t) = f_i(t) - (m+\mu)\, \ddot{u}_i \tag{5.32}$$

$$= \lambda \frac{d^2}{dt^2} \cos\theta_i. \tag{5.33}$$

This permits me to identify a spectral power density:

$$\Pi(\omega) = \frac{-1}{\pi} \Im \left(\sum_{i,j} \omega\, \tilde{q}_i^*(\omega)\, \tilde{g}_{ij}(\omega)\, \tilde{q}_j(\omega) \right). \tag{5.34}$$

Spectral power density can be evaluated as a function of frequency by short-time Fourier transform over data from the numerical solutions, as in figure 5.8. In that figure, the frequency resolution $\Delta\omega$ is $(2\pi/4096)$ rad/s, corresponding to time records with 4096 samples.

The subfigures in figure 5.8 correspond to the labels in figure 5.7(a). Subfigures (a) through (e) show that the power output is strong and confined to one or two narrow peaks. The width of the peaks appears to be governed by the resolution of the discrete Fourier transform. Subfigure (b) is of particular interest since it indicates lasing in two modes simultaneously, like a multimode laser. In subfigure (f), the power output is weak, broadband, and noisy. The small differences in mean natural motor speed across subfigures (d-f) show that transitions between the various states can be abrupt. This corresponds to the

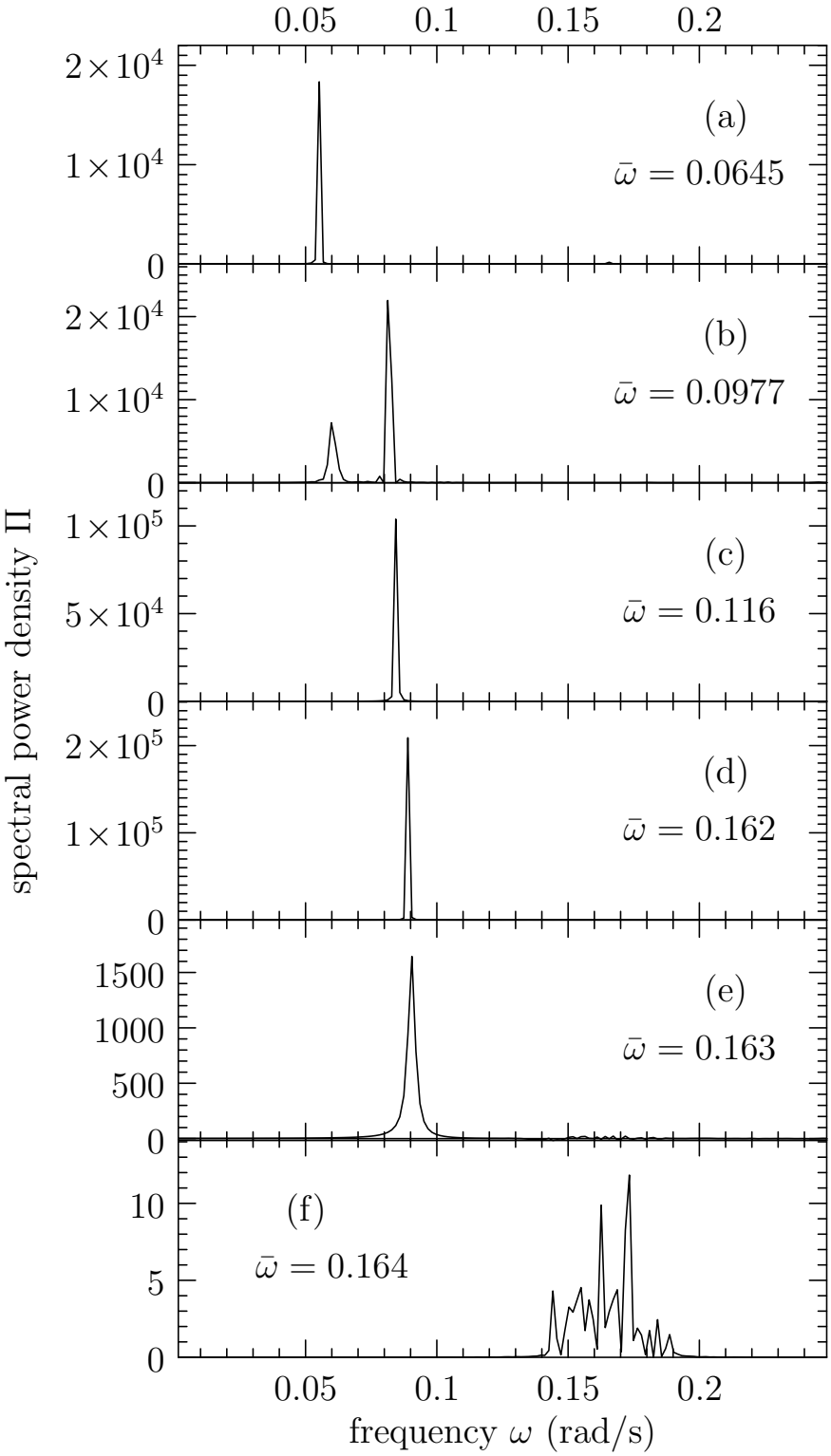

Figure 5.8: Spectral power density vs frequency. The data for these figures are from the same upward run as the data in figure 5.7(a) and correspond to the labels in that figure. The means of the natural speeds are indicated in each subfigure. Note that the differences in natural speeds among subfigures (d-f) are small—the transition is abrupt.

sudden changes in audible power output observed in the last Chapter and is reminiscent of a lasing transition.

The frequency at which $\Pi(\omega)$ peaks, as shown in figure 5.8, is not always the same as the average motor speed Ω shown in figure 5.7. Consider the cases (d) and (e), for which $\bar{\omega} = 0.162$ and 0.163 rad/s. The dash-dotted line in figure 5.7 indicates a measured average motor speed Ω of about 0.095 rad/s whereas the power output in subfigures (d) and (e) of figure 5.8 show peaks just below the resonant frequency, 0.09 rad/s. The peak of the power output is biased towards the motors operating near a resonance, making the frequency of the maximum power output distinct from the average motor speed. (Note that I developed the normalization procedure in the last Chapter to solve precisely this problem. However, the procedure that I detailed only works when the motors couple to the plate equally, a situation that requires a carefully chosen geometry.)

5.4 Conclusion

The main features of the laboratory observations presented in the previous Chapter include bistability, hysteresis, and a spectral gap. The original Kuramoto model is unable to describe this behavior. However, the first-principle model that I develop in this Chapter shows that with only a couple of modifications to the Kuramoto model, I can reproduce those features. I also find theoretical evidence that the laboratory system should exhibit stimulated emission and superradiance, and therefore should serve as an acoustic analog to a laser.

Chapter 6

Final Remarks

Synchronization is an engaging and intuitive subject, and the Kuramoto model is a simple model for that subject. This dissertation details my contribution to the field of synchronization. As reflected in the structure of the document, I view my work as two distinct projects aimed at different aspects of the field.

My theoretical studies of synchronization have focused on making population-specific predictions for the Kuramoto model by assuming a mean field $r\,e^{\imath\psi}$ that has a constant magnitude and a constant rate of rotation. By taking the rate of rotation as a parameter of the self-consistent solution for r, I have shown that I can obtain excellent predictions for the value of r for both symmetric and unsymmetric populations. The quality of the predictions varies from population to population, but generally gets better as K increases. In particular, for K larger than the coupling of the largest discontinuity, the predictions consistently perform well.

My experimental studies of synchronization have focused on exploring the collective behavior of oscillators that couple through a resonant medium. Cell-phone vibrators glued to a plate interact with each other through that plate, and the strength of the coupling depends on the resonant characteristics of the plate. The resulting collective behavior exhibits the properties that motor synchronization preferentially occur rs at frequencies close to but below the resonant frequencies of the plate. Multiple stable synchronization frequencies are possible for the same driving voltage and generally lead to hysteresis in collective behavior. The motors even serve as an acoustic analog to a laser, exhibiting stimulated emission and super-radiance.

Even after studying synchronization intensely for over three years, I have many unanswered questions. The most important question related to my work in the first part of this dissertation is whether real finite-sized Kuramoto systems exhibit finite discontinuities in their order parameters. I have preliminary numerical evidence that indicates that some populations of $N = 4096$ exhibit switching behavior between two different states. The behavior is swift, almost Markovian, and symmetric populations show a much higher likelihood of such behavior. And, the scheme predicted a jump for a K value in the neighborhood of the switching behavior. Is this a general feature, and does the scheme generally correspond with such behavior for larger systems? Do these discontinuities exhibit critical scaling?

From a more theoretical angle, I wonder if the large-N integral form for the full scheme could give meaningful predictions for the order parameter for skewed populations. I also wonder if the scheme could be improved by attempting to compute the spectrum of fluctuations in r self-consistently.

The experimental work also has many avenues of further work. The unsynchronized behavior looks very interesting: is it chaotic or just noisy? I have shown here how the motors respond to resonances when they interact with the plate modes in an identical fashion, but what about different motor layouts or plate geometries? Can the theory be extended to handle these more complex Green functions? At one point the theory assumed that all the oscillators run at identical natural speeds. Can this substantial restriction be relaxed?

Answers to all of these questions are beyond the scope of this work, but I look forward to the future science that will bring answers to all of these questions—and raise new questions of their own.

Bibliography

[1] Steven Strogatz, Daniel Abrams, Allan McRobie, Bruno Eckhardt, and Edward Ott. Theoretical mechanics: Crowd synchrony on the Millennium Bridge. *Nature*, 438:43–44, November 2005.

[2] Daniel Abrams. *Two coupled oscillator models: the Millennium Bridge and the chimera state*. PhD thesis, Cornell University, July 2006.

[3] Steven H. Strogatz and Renato E. Mirollo. Stability of incoherence in a population of coupled oscillators. *J. Stat. Phys.*, 63(3/4):613–635, 1991.

[4] Y. Kuramoto and D. Battogtokh. Coexistence of coherence and incoherence in nonlocally coupled phase oscillators. *Nonlinear Phenomena in Complex Systems*, 5(4):380–385, 2002.

[5] Danial M. Abrams and Steven H. Strogatz. Chimera states for coupled oscillators. *Phys. Rev. Lett.*, 93:174102, October 2004.

[6] Daniel M. Abrams and Steven H. Strogatz. Chimera states in a ring of nonlocally coupled oscillators. *Int. J. Bifurcation and Chaos*, 16(1):21–37, 2006.

[7] Daniel M. Abrams, Rennie Mirollo, Steven H. Strogatz, and Daniel A. Wiley. Solvable model for chimera states of coupled oscillators. *Phys. Rev. Lett.*, 101:084103, August 2008.

[8] Tony E. Lee, Heywood Tam, G. Refael, Jeffrey L. Rogers, and M. C. Cross. Vortices and the entrainment transition in the two-dimensional kuramoto model. *Phys. Rev. E*, 82(3):036202, Sep 2010.

[9] Arthur T. Winfree. Biological rhythms and the behavior of populations of coupled oscillators. *J. Theor. Biol.*, 16:15–42, 1967.

[10] Y. Kuramoto. *Self-Entrainment of a Population of Coupled Nonlinear Oscillators*, volume 39 of *Lecture Notes in Physics*, page 420. Springer-Verlag, 1975.

[11] John Crawford. Amplitude expansions for instabilities in populations of globally-coupled oscillators. *J. Stat. Phys.*, 74(5/6):1047–1084, 1994.

[12] Edward Ott and Thomas. M. Antonsen. Low dimensional behavior of large systems of globally coupled oscillators. *Chaos*, 18(3):037113–1–037113–6, September 2008.

[13] S. H. Strogatz. From Kuramoto to Crawford: exploring the onset of synchronization in populations of coupled oscillators. *Physica D*, 143:1–20, 2000.

[14] Hidetsugu Sakaguchi and Yoshiki Kuramoto. A soluble active rotator model showing phase transitions via mutual entrainment. *Prog. Theor. Phys.*, 76(3):576–581, September 1986.

[15] R. Adler. A study of locking phenomena in oscillators. *Proc IEEE*, 61:351–357, 1946.

[16] Nigel Goldenfeld. *Lectures on Phase Transitions and the Renormalization Group*, volume 85 of *Frontiers in Physics*. Westview Press, 1992.

[17] P. C. Hohenberg and B. I. Halperin. Theory of dynamic critical phenomena. *Reviews of Modern Physics*, 49(3):435–479, July 1977.

[18] Hiroaki Daido. Discrete-time population dynamics of interacting self-oscillators. *Progress in Theoretical Physics*, 75(6):1460–1463, June 1986.

[19] Hiroaki Daido. Scaling behavior a the onset of mutual entrainment in a population of interacting oscillators. *Journal of Physics A*, 20:L629–L636, 1987.

[20] Hiroaki Daido. Lower critical dimension for populations of oscillators with randomly distributed frequencies: A renormalization-group approach. *Physical Review Letters*, 61(2):231–234, July 1988.

[21] H. Daido. Intrinsic fluctuation and its critical scaling in a class of populations of oscillators with distributed frequencies. *Prog. Theor. Phys.*, 81(4):727–731, April 1989.

[22] Hiroaki Daido. Intrinsic fluctuations and a phase transition in a class of large populations of interacting oscillators. *Journal of Statistical Physics*, 60:753–799, 1990.

[23] Yoshiki Kuramoto and Ikuko Nishikawa. Statistical macrodynamics of large dynamical systems. case of a phase transition in oscillator communities. *Journal of Statistical Physics*, 49:569–605, 1987.

[24] Arkady Pikovsky and Stefano Ruffo. Finite-size effects in a population of interacting oscillators. *Physical Review E*, 59(2):1633–1636, February 1999.

[25] Olga Perković, Karin A. Dahmen, and James P. Sethna. Disorder-induced critical phenomena in hysteresis: A numerical scaling analysis. arXiv, 1996.

[26] John Buck. Synchronous rhythmic flashing of fireflies. *Q. Rev. Biol.*, 13(3):301–314, September 1938.

[27] Anton Burykin and Timothy G. Buchman. Cardiorespiratory dynamics during transitions between mechanical and spontaneous ventilation in intensive care. *Complexity*, 13(6):40–59, 2008.

[28] William S. Bush and Hava T. Siegelman. Circadian synchrony in networks of protein rhythm driven neurons. *Complexity*, 12(1):67–72, 2006.

[29] James Pantaleone. Synchronization of metronomes. *Am. J. Phys.*, 70(10):992–1000, October 2002.

[30] S. Yu. Kourtchatov, V. V. Likhanskii, A. P. Napartovich, F. T. Arecchi, and A. Lapucci. Theory of phase locking of globally coupled laser arrays. *Phys. Rev. A*, 52(5):4089–4094, November 1995.

[31] Y. Kuramoto. *Chemical Oscillations, Waves, and Turbulence.* Springer-Verlag, New York, 1984.

[32] I. Z. Kiss, Y. Zhai, and J. L. Hudson. Emerging coherence in a population of chemical oscillators. *Science*, 296:1676–1678, May 2002.

[33] Istvan Z. Kiss, Yumei Zhai, and John L. Hudson. Resonance clustering in globally coupled electrochemical oscillators with external forcing. *Phys. Rev. E*, 77:046204–1 to 046204–7, 2008.

[34] Montserrat A. Miranda and Javier Burguete. Spatiotemporal phase synchronization in a large array of convective oscillators. *Int. J. Bifurcation and Chaos*, 20(3):835–847, 2010.

[35] Kwok Yeung Tsang, Renato E. Mirollo, Steven H. Strogatz, and Kurt Weisenfeld. Dynamics of a globally coupled oscillator array. *Physica D*, 48:102–112, 1991.

[36] G. W. Swift. Thermoacoustic engines. *J. Acoust. Soc. Am.*, 84:1145–1180, 1988.

[37] P. S. Spoor and G. W. Swift. Mode-locking of acoustic resonators and its application to vibration cancellation in acoustic heat engines. *J. Acoust. Soc. Am.*, 106:1353–1362, 1999.

[38] P. S. Spoor and G. W. Swift. The huygens entrainment phenomenon and thermoacoustic engines. *J. Acoust. Soc. Am.*, 108:588–599, 2000.

[39] P. Barbara, A. B. Cawthorne, S. V. Shitov, and C. J. Lobb. Stimulated emission and amplification in Josephson junction arrays. *Physical Review Letters*, 82:1963–1966, 1999.

[40] P. Hadley, M. R. Beasly, and K. Wiesenfeld. Phase locking in Josephson-junction series arrays. *Phys. Rev. B*, 38:8712–8719, 1988.

[41] K. Wiesenfeld, P. Colet, and S. H. Strogatz. Synchronization transitions in a disordered Josephson series array. *Physical Review Letters*, 76:404–407, 1996.

[42] Kurt Weisenfeld, Pere Colet, and Steven H. Strogatz. Frequency locking in Josephson arrays: Connection with the Kuramoto model. *Phys. Rev. E*, 57(2):1563–1569, February 1998.

[43] B. Bennett, M. F. Schatz, H. Rockwood, and K. Wiesenfeld. Huygens' clocks. *Proc. Roy. Soc., Series A-Mathematical physical and engineering sciences*, 458:563–579, 2002.

[44] M. K. Stephen Yeung and Steven H. Strogatz. Time delay in the Kuramoto model of coupled oscillators. *Physical Review Letters*, 82(3):648–651, January 1999.